Reconfigurable and Static EM Skins on Vehicles for Localization

Dario Tagliaferri, *Member, IEEE*, Marouan Mizmizi, *Member, IEEE*, Giacomo Oliveri, *Fellow, IEEE*, Umberto Spagnolini, *Senior Member, IEEE* and Andrea Massa, *Fellow, IEEE*

***Abstract*—Electromagnetic skins (EMSs) have been recently considered as a booster for wireless sensing, but their usage on mobile targets is relatively novel and could be of interest when the target reflectivity can/must be increased to improve its detection or the estimation of parameters. In particular, when illuminated by a wide-bandwidth signal (e.g., from a radar operating at millimeter waves), vehicles behave like *extended targets*, since multiple parts of the vehicle's body effectively contribute to the back-scattering. Moreover, in some cases perspective deformations challenge the correct localization of the vehicle. To address these issues, we propose lodging EMSs on vehicles' roof to act as high-reflectivity planar retro-reflectors toward the sensing terminal. The advantage is twofold: *(i)* by introducing a compact high-reflectivity structure on the target, we make vehicles behave like *point targets*, avoiding perspective deformations and related ranging biases and *(ii)* we increase the reflectivity of the vehicle, improving localization performance. We detail the EMS design from the system-level to the full-wave-level considering both reconfigurable intelligent surfaces (RIS) and cost-effective static passive electromagnetic skins (SP-EMSs). Localization performance of the EMS-aided sensing system is also assessed by Cramér-Rao bound analysis in both narrowband and spatial wideband operating conditions.**

***Index Terms*—Metasurfaces, RIS, Electromagnetic Skins, Vehicles, Localization, Cramér-Rao bound**

I. Introduction

Localization is a fundamental pre-requisite for many applications and use-cases of the sixth generation of communication systems (6G), which is expected to enable novel market verticals such as automated driving, augmented reality, high-fidelity digital twins of the physical environment and others [1]. High-accuracy localization (i.e., below 10 cm of accuracy [2]) is supported by the release of large bandwidths in the millimeter wave (mmWave) and sub-THz portions of the EM spectrum (< 300 GHz) [3], as well as by the use of massive antenna arrays, either dedicated to sensing purposes (e.g., radars) or already in place for communication. Electromagnetic skins (EMSs) are surging as one of the promising technologies for 6G, boosting communication performance as well as localization, as recently shown [4]. An EMS is generally defined as any surface capable of EM wave manipulation beyond Snell's law of reflection/refraction [5]. In this framework, several technologies are emerging to implement this functionality, including reconfigurable intelligent surfaces (RISs). Such devices consist of a collection of sub-wavelength-sized passive elements, called *meta-atoms*, whose complex reflection coefficients can be electronically tuned to manipulate the incident and reflected/refracted wavefronts [6]. From the localization perspective, RISs can be designed to operate as anomalous mirrors to extend the range in non-line-of-sight (NLOS) [7] or to improve the angular diversity by magnifying the transmitter (Tx) or receiver (Rx) aperture [8]. Hence, boosting the estimation of position and orientation of one or multiple targets. In the following, we revise the state of the art on EMSs used for localization and we then outline the contributions of this work.

A. Literature Survey

The literature on RIS-aided localization underwent significant growth in the last few years [9]. In [10], [11], the authors propose to use a RIS to assist radar in NLOS conditions, addressing the maximization of the probability of correct detection of a given target, via signal-to-noise (SNR) maximization with constrained phase design. The results analyze the

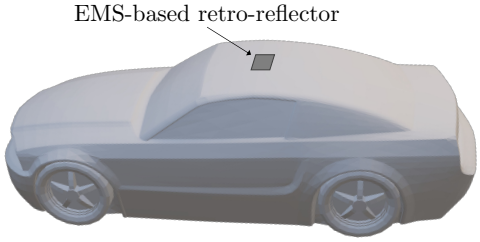

Fig. 1: EMS-based retro-reflector on the roof of the vehicle for localization purposes

This work was partially supported by the European Union under the Italian National Recovery and Resilience Plan (NRRP) of NextGenerationEU, partnership on "Telecommunications of the Future" (PE00000001 - program "RESTART").

D. Tagliaferri, M. Mizmizi, U. Spagnolini are with the Department of Electronics, Information and Bioengineering (DEIB) of Politecnico di Milano, 20133 Milan, Italy (e-mail: [dario.tagliaferri, marouan.mizmizi, umberto.spagnolini]@polimi.it

U. Spagnolini is Huawei Industry Chair

G. Oliveri is with the ELEDIA Research Center (ELEDIA@UniTN - University of Trento), DICAM - Department of Civil, Environmental, and Mechanical Engineering, Via Mesiano 77, 38123 Trento - Italy (email: giacomo.oliveri@unitn.it)

A. Massa is with the ELEDIA Research Center (ELEDIA@UESTC-UESTC), School of Electronic Science and Engineering, University of Electronic Science and Technology of China (UESTC), Chengdu 611731, China, also with the ELEDIA Research Center (ELEDIA@UniTN - University of Trento), DICAM - Department of Civil, Environmental, and Mechanical Engineering, Via Mesiano 77, 38123 Trento - Italy, also with the ELEDIA Research Center (ELEDIA@TSINGHUA - Tsinghua University), Beijing100084, China, also with the School of Electrical Engineering, Tel Aviv University, Tel Aviv 69978, Israel (e-mail: andrea.massa@unitn.it).

Cramér Rao bound (CRB) on position estimation and suggest the placement of the RIS near either the radar or the target, to combat the severe path loss induced by a double or triple reflection (Tx-RIS-target-RIS-Rx). The same authors extend the previous works to the usage of active RIS, hence taking into account architectures with amplification capabilities [12]. The authors of [13] analyze the CRB-derived position and orientation error bounds on a RIS-aided localization system, showing numerical results and proposing a suitable CRB-minimizing phase design approach. Radar surveillance in NLOS scenarios assisted by RIS is proposed in [14], whereby different operating regimes of the RIS are discussed. The work in [15] proposes a RIS-aided localization system in cellular networks, while [16] focus on the same scenario and it exploits a machine learning approach. Differently, the work [17] considers an indoor scenario. The works [18], [19] consider indoor user localization employing RIS and received signal strength measurements. Paper [20] compares the localization performance of RIS-aided and continuous EMSs-aided integrated sensing and communication (ISAC) systems, deriving the CRB in both cases. The paper [21] proposes to adopt a two-timescale phase design approach in ISAC systems to reduce the signaling overhead to acquire the channel state information (CSI) at the RIS. RIS phases are kept constant during the location coherence interval of the user/target while the precoder at the base station varies according to the communication channel coherence time. The authors of [22] address the problem of RIS modeling mismatch in RIS-aided localization, namely deriving the misspecified CRB on positioning performance for the case in which the system assumes the RIS to have a phase-only control (and unit amplitude) while the true reflection coefficient has non-negligible amplitude variation with the incidence angle.

Recently, research advances on EMSs shifted towards large implementations (whose size is comparable with the propagation distance) to boost both communication and localization performance by increasing the effective aperture [23]. With the increased aperture, literature works started to explore the challenges and possibilities of the near-field operation, namely the additional degrees of freedom brought by a non-planar wavefront across the RIS [24]. The authors of [25] derive the fundamental position error bounds for near-field RIS-aided localization systems. The paper [26] addresses the near-field target localization in NLOS scenarios, evaluating the CRB on position estimation and proposing an optimization problem to design the RIS phases for CRB minimization. The work [27] exploits the near-field-operating RIS as a localization enabler for a single-antenna terminal that is willing to localize a target in the environment. The authors deal with the multipath problem by leveraging compressed sensing algorithms. The authors of [28] consider a hybrid RIS, where a limited number of RF chains at the RIS enables basic signal processing on the received signal.

Previous works assume that RISs are statically placed in the environment, e.g., on the building facades, magnifying the Tx/Rx aperture to improve localization accuracy. Very few works consider the possibility of directly placing the RIS on targets, to facilitate their localization [29]–[31]. For instance, the authors of [29] exploit one Tx terminal and multiple asynchronous Rx stations to localize users equipped with RIS via time-of-arrival estimation. A phase design is proposed and the simulation results are compared with the CRB on 3D position estimation. The same authors extended the previous work to near-field operating conditions in [30]. More recently, the authors of [31] consider the estimation of the position and orientation of a target-mounted RIS (lodged on an unmanned aerial vehicle), deriving the CRB on position and orientation. The aforementioned works only considered a *narrowband* RIS operation, namely a frequency-flat RIS reflection model over the whole Tx signal bandwidth. In most sensing scenarios, however, the available bandwidth is large enough to induce *spatial wideband* effects at the RIS, namely a frequency-selective RIS response within the bandwidth of interest. An increased bandwidth generally enhances localization performance, but spatial wideband effects in far-field lead to the so-called beam squinting, namely each frequency component of the impinging signal on the RIS is reflected towards a different angular direction, due to the mismatch between the wavelength at which the RIS is manufactured (λ_0) and the impinging one ($\lambda \neq \lambda_0$) [32]. A similar effect (defocusing) is observed when the RIS is in the near-field of the sensing terminal and/or vice-versa [33]. Therefore, current literature on target-lodged RIS, such as [29]–[31], does not fully capture the RIS reflection behavior for wide bandwidth localization systems, that is the focus of this work.

B. Contribution

This paper focuses on the usage of EMSs to improve vehicles' localization when illuminated from above by a wide bandwidth (GHz-wide) sensing signal, such as an ISAC terminal or a multiple-input-multiple-output (MIMO) radar. When the resolution cell of the sensing system is much smaller than the vehicle size, the latter behaves like an *extended target*, challenging its localization and tracking [34], [35]. Moreover, when the sensing terminal is above the vehicle, perspective deformations such as overlay and foreshortening hinder the correct localization of the vehicle from sensing data, as double bounces with the vehicle and the ground bias the time-of-arrival measurements [36]. In this setting, we propose to lodge an EMS on the top side of ground vehicles (Fig. 1) to assist radar localization by acting as an omnidirectional retro-reflector. Indeed, any part of the vehicle can be in principle coated with EMSs, provided that the EMS adheres to the surface's shape, that can be non-planar. In our previous works, we explored such conformal EMSs for communication purposes, studying the advantages for opportunistic relaying to overcome link blockage in vehicular networks [37]–[39]. The proposed work, instead, considers lodging EMSs on the flat vehicle's roof with a specific focus on sensing. The advantage of the latter approach twofold: *(i)* the EMS increases the reflectivity of the vehicle, thus its radar cross section (RCS) and hence its *visibility* in sensing data and *(ii)* with a proper EMS design, the vehicle behaves like a *point target*, allowing the detection, localization, and tracking of a single, known region of the vehicle (e.g., the

position of the mmWave communication transceiver of the roof). Examples of realization of EMS-based retro-reflectors at mmWave/THz bands are present in literature [40], but this paper considers that the EMS operates in mobility, and its dynamic configuration is investigated herein.

The main contributions of the paper are as follows:

- The motivation for the usage of EMSs for vehicle localization is clarified with an experimental radar data acquisition campaign. We employ a Texas Instrument high-resolution mmWave radar mounted at 8 m from the ground that illuminates a traveling vehicle. Through experiments, we demonstrate the severe perspective deformations in the radar image of the vehicle, and we demonstrate the benefits of having EMSs acting as *EM markers* on vehicles' roofs.
- We propose a RIS-based retro-reflector design for vehicles. RIS phases are set to enable intentional retro-reflection of the impinging sensing signal towards the sensing terminal. With the aforementioned experimental tests, we empirically derive the minimum radar cross section (RCS) required for the RIS (thus its physical size) to make it detectable in the sensing data. Then, we show that an inaccurate RIS phase design, e.g., only based on coarse vehicle's positioning (such as GPS), leads to a drastic reduction of the average RCS of several dBm^2 due to reflection misalignment with the impinging sensing signal. To obviate the latter issue, a dynamic RIS-alignment sweeping procedure is detailed, designing the phase of the RIS elements as a function of *(i)* the coarse vehicle's position estimate w.r.t. the sensing terminal, *(ii)* the uncertainty on vehicle's position estimate and *(iii)* the beamwidth of the RIS reflection pattern. Mobility considerations are added and discussed.
- To decrease the implementation cost and complexity of a RIS-based reflector, the paper proposes a novel design based on static-passive EM skins (SP-EMSs), an inexpensive solution (two/three orders of magnitude less w.r.t. RISs) to enable advanced wave manipulation and anomalous reflection capabilities, obtained by tailoring the micro-scale geometric/physical properties of the meta-atom comprised in the artificial surface [41]–[43]. SP-EMSs are pre-configured, thus we design the wideband omnidirectional retro-reflector by combining multiple, differently configured modules. The design of the single SP-EMS module is validated with full-wave simulations with high-frequency structure simulation (Ansys HFSS).
- Localization performance for EMS-equipped vehicles is evaluated by CRB on joint vehicle position estimation and RIS phase configuration uncertainty, for both frequency-dependent (spatial wideband) and frequency-flat (narrowband) RIS behavior. We compare the case in which the phase configuration of the RIS is deterministic (but unknown), or random, with *a-priori* information brought by coarse positioning at the vehicle side. In the former case, we employ the CRB, while the latter is addressed with hybrid CRB (HCRB) [44]. The results highlight the importance of spatial wideband RIS modeling, as its frequency-dependent behavior acts as a filter on the spectrum of the impinging signal. In some cases, severe position-dependent filtering on the impinging signal contributes to a decrease in the CRB compared to the narrowband RIS behavior. Localization performance is compared against the case of a bare vehicle (without the EMS), showing the promising performance gap of using an EMS.

Organization: The paper is organized as follows: Section II shows the experimental results aimed at motivating the usage of vehicle-lodged EMSs for localization, Section III outlines the system model, Sections IV and V reports the design of RIS- and SP-EMS-based reflector, respectively, Section VI shows the localization performance using RISs/SP-EMSs while Section VII concludes this work.

Notation: Bold upper and lower-case letters stand for matrices and column vectors, respectively. $[\mathbf{A}]_{(i,j)}$ denotes the (i,j) entry of matrix $\mathbf{A}$. Matrix transposition and conjugate transposition of $\mathbf{A}$ are indicated as $\mathbf{A}^T$ and $\mathbf{A}^H$, respectively. $\mathbb{E}$ denotes the expectation operator. With $\mathbf{a} \sim \mathcal{CN}(\boldsymbol{\mu}, \mathbf{C})$ we denote a circularly complex multi-variate Gaussian random variable with mean $\boldsymbol{\mu}$ and covariance matrix $\mathbf{C}$. With $a \sim \mathcal{U}[b,c]$ we denote a uniformly distributed random variable between b and c. $\mathcal{A}\times\mathcal{B}$ denotes the Cartesian product between sets $\mathcal{A}$ and $\mathcal{B}$. $\mathbb{R}$ and $\mathbb{C}$ denote, respectively, the set of real and complex numbers. δ_n is the Kronecker delta function.

II. Problem Formulation and Methodology

Localizing the vehicle from a generic sensing terminal means estimating its position and possibly orientation based on the back-scattered signal. When the sensing terminal is located at the communication infrastructure (e.g., ISAC base stations (BSs) or MIMO radar), its height compared to the one of the target is large, typically $8-25$ m for a BS [45] and $1.5-1.7$ m for a generic vehicle. When vehicles are illuminated from above, they back-scatter the incident radio signal depending on their geometric shape and location w.r.t. the sensing terminal. Typically, the resulting sensing image for these extended targets is subject to *(i)* perspective deformations, referred to as overlay and foreshortening, which distort the true target's geometry [36] and *(ii)* double bounce with

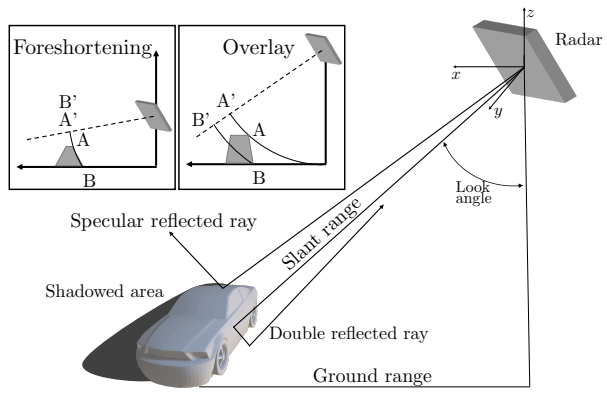

Fig. 2: Perspective deformations and double bounces in the generated sensing image.

This article has been accepted for publication in IEEE Transactions on Wireless Communications. This is the author's version which has not been fully edited and content may change prior to final publication. Citation information: DOI 10.1109/TWC.2024.3437778

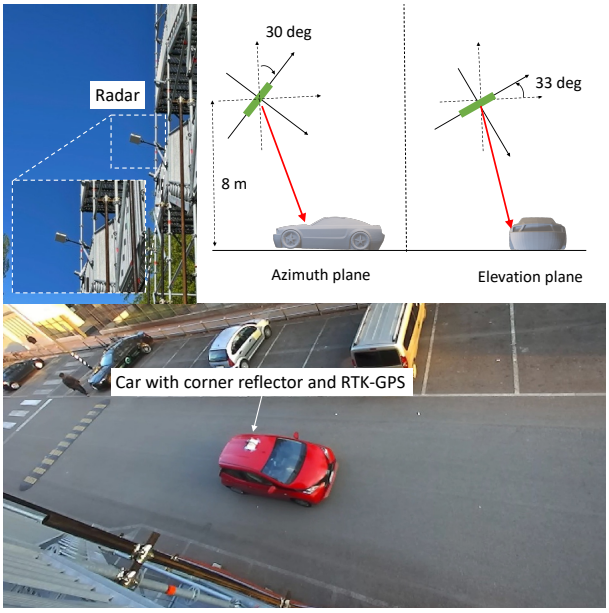

Fig. 3: Experimental setup: a MIMO radar located at 8 m height illuminates the street below where a car is purposely equipped with a corner reflector

the ground, that biases the time-of-arrival and leads to ghost targets at farther range in the generated image. Fig. 2 depicts both the aforementioned effects.

To gain further insight into these effects and to motivate the use of vehicle-lodged EMSs, we report an example from an extensive radar data acquisition campaign mimicking a radar-/ISAC- BS sensing the surroundings. The geometry of the acquisition is shown in Fig. 3, where a MIMO radar operating at 77 GHz frequency, with bandwidth $B = 2.5$ GHz (range resolution of 6 cm) and azimuth resolution of 1.4 deg is located at 8 m height above the road and illuminates the street below, where a car is traveling along a straight path at constant velocity. The true trajectory of the car for comparison is obtained using a real-time kinematic global positioning system (RTK-GPS) placed on the car roof.

The radar image in Fig. 4a shows two superimposed frames, with the vehicle being in a lateral position and subsequently in a central one (below the radar). The white dashed line is the true trajectory of the car, measured with a real-time kinematic (RTK) positioning setup, herein identified as the position of a possible mmWave/sub-THz antenna (notice that linear trajectory is curved in the slant-range plane). One can observe that the vehicle in the central position (rightmost and closest frame) reflects only with the lateral side, predominantly from the wheels and the alloy rims. A significant contribution to the back-scatter comes from double bounce with the asphalt. The zoomed picture in Fig. 4 shows a shadowed area due to the vehicle's silhouette (objects in this area are not visible to the radar). Instead, when the vehicle is in the lateral position, it reflects with the frontal-lateral corner side. In addition, we observe that the wheels appear farther away than the roof. These effects are the aforementioned foreshortening and layover, mixed with the double-bounce effect, requiring accurate a-priori information on both the geometry and the

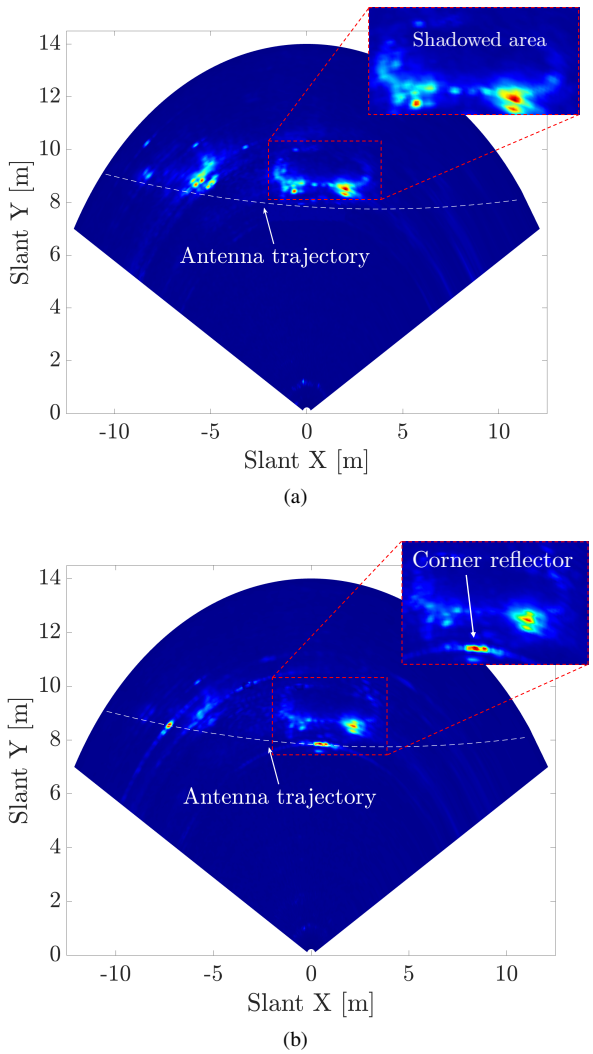

Fig. 4: Example of radar image of a car in slant range for (4a) bare car and (4b) car equipped with a corner reflector.

physical structure of the target to be compensated for. If we are interested in the localization of a single, preferred point of the vehicle, for instance, the location of the mmWave/sub-THz antenna, having such an extended target whose peak reflectivity shifts according to the specific position in space requires advanced yet complicated tracking algorithms operating on raw radar data [35], [46]–[48].

To facilitate the localization of the vehicle, this paper proposes to mount a reflector on the roof of the connected vehicles. To illustrate the potential of the proposed idea, we equipped the car with a four-sided corner reflector at the center of the roof, each side with 10×10 cm^2 area. Fig. 4b represents the superposition of two radar frames, and it outlines that the corner reflector is visible in the radar image allowing for a precise localization. In other words, the vehicle behaves like a *point target* in the slant-range acquisition frame. Nevertheless, mounting a corner reflector on the car's roof is neither aesthetic nor practical, as it may interfere with the vehicle's aerodynamics. Hence, we propose to use EMSs as planar omnidirectional reflectors (*EM markers*), which can

better adapt to the car's roof shape. In the following sections, the design of omnidirectional reflectors based on EMSs is discussed.

III. System Model

Let us consider a vehicle mounting a rectangular EMS on the roof and a sensing terminal (e.g., an ISAC BS, a MIMO radar) that aims at localizing the vehicle via localizing the EMS. In the most general case, the sensing terminal implements L measurement channels, i.e., a transmitting (Tx)-receiving (Rx) antenna pair. For the ℓ-th Tx-Rx channel, the sensing terminal emits the pass-band signal:

$$g_{\mathrm{Tx},\ell}(t) = s_{\mathrm{Tx},\ell}(t)e^{j2\pi f_0 t} \tag{1}$$

where $s_{\mathrm{Tx},\ell}(t)$ is the Tx antenna-specific base-band waveform of bandwidth B and the carrier frequency is denoted by f_0. Signal $s_{\mathrm{Tx},\ell}(t)$ can be intentionally (as for radar) or occasionally (as for ISAC) generated. Here, we assume orthogonal waveforms, as common for radar systems operating in time- or code-division multiplexing [49].

The geometry of the system is sketched in Fig. 5. The sensing terminal is located in the origin of the *global* reference system (position of the phase center), and the Tx and Rx antennas are deployed over the yz plane. The 3D positions of Tx and Rx antennas forming the ℓ-th channel are denoted as $\mathbf{s}_\ell \in \mathbb{R}^{3\times 1}$ and $\mathbf{r}_\ell \in \mathbb{R}^{3\times 1}$, respectively. The planar EMS is in the generic position $\mathbf{x} = [x, y, z]^T \in \mathbb{R}^{3\times 1}$, whose estimation is the objective of the EMS localization, and it is made by $N \times M$ elements. The EMS defines a *local* reference system in which the $N \times M$ EMS elements lie on the $x'y'$ plane. The axes of the local reference system are rotated w.r.t. the global ones by the vehicle's heading ψ. Therefore, the position of the (n, m)-th element in global coordinates is:

$$\mathbf{x}_{nm} = \mathbf{x} + \mathbf{Q}_z(\psi)\mathbf{p}_{nm} \tag{2}$$

for $n = -N/2, ..., N/2-1$, $m = -M/2, ..., M/2-1$, where $\mathbf{p}_{nm} = [nd,\, md,\, 0]^T$ is the position of the (n, m)-th element in local coordinates, with d being the inter-element spacing. Matrix

$$\mathbf{Q}_z(\psi) = \begin{bmatrix} \cos\psi & -\sin\psi & 0 \\ \sin\psi & \cos\psi & 0 \\ 0 & 0 & 1 \end{bmatrix} \tag{3}$$

defines the relative counterclockwise rotation of the local reference system around z axis by angle ψ.

A. System Model in Time Domain

The expression of the Rx signal at the ℓ-th measurement channel of the sensing terminal can be expressed as in (4), where:

- factor $\rho \in \mathbb{C}$ includes geometrical energy losses as well as the antenna gains at the sensing terminal and the single-element gain of the EMS;
- $s(t) = s_{\mathrm{Tx},\ell}(t) * s^*_{\mathrm{Tx},\ell}(-t)$ is the range-compressed pulse, independent on the specific channel;
- Φ_{nm} denotes the phase applied at the (n, m)-th element of the EMS;

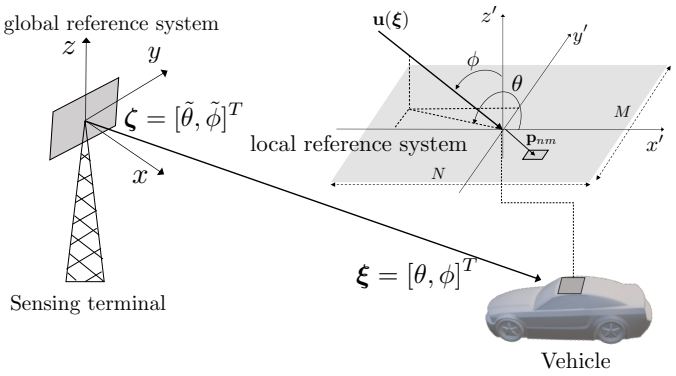

Fig. 5: Global and EMS-local reference systems.

- $\tau^i_{\ell,nm}$ and $\tau^o_{\ell,nm}$ indicate the forward and backward propagation delays, computed as

$$\tau^i_{\ell,nm} = \frac{\|\mathbf{x}_{nm} - \mathbf{s}_\ell\|}{c}, \quad \tau^o_{\ell,nm} = \frac{\|\mathbf{r}_\ell - \mathbf{x}_{nm}\|}{c}; \tag{5}$$

- $z_\ell(t) \in \mathcal{CN}(0, \sigma_z^2\delta_{\ell-k}\delta(t))$ is the additive white noise, uncorrelated over different channels.

The first, exact expression in (4) describes the most general case in which the wavefront across the EMS is non-planar, thus the EMS is in near-field w.r.t. the sensing terminal, and the same condition applies to the retro-reflected signal at the sensing terminal. This modeling is general but often can be simplified by constraining the geometry of the problem.

Approximation (a) in (4) assumes that the size of the EMS compared to the propagation distance is small, such that the incidence and reflected wavefront at both the sensing terminal and the EMS can be approximated as planar (*far-field*). In far-field, the delays can be linearized as follows:

$$\tau^i_{\ell,nm} \simeq \underbrace{\frac{\|\mathbf{x}\|}{c}}_{\tau_0} + \underbrace{\frac{\mathbf{s}_\ell^T\mathbf{u}(\boldsymbol{\zeta})}{c}}_{\Delta\tau^i_\ell} + \underbrace{\frac{\mathbf{p}_{nm}^T\mathbf{u}(\boldsymbol{\xi})}{c}}_{\Delta\tau_{nm}(\boldsymbol{\xi})} \tag{6}$$

$$\tau^o_{\ell,nm} \simeq \underbrace{\frac{\|\mathbf{x}\|}{c}}_{\tau_0} + \underbrace{\frac{\mathbf{r}_\ell^T\mathbf{u}(\boldsymbol{\zeta})}{c}}_{\Delta\tau^o_\ell} + \underbrace{\frac{\mathbf{p}_{nm}^T\mathbf{u}(\boldsymbol{\xi})}{c}}_{\Delta\tau_{nm}(\boldsymbol{\xi})}, \tag{7}$$

where τ_0 is the one-way propagation delay from the phase center of the sensing terminal to the phase center of the EMS, $\Delta\tau^i_\ell$, and $\Delta\tau^o_\ell$ are the residual (excess) delays at the sensing terminal w.r.t. to its phase center and, similarly, $\Delta\tau_{nm}(\boldsymbol{\xi})$ is the excess propagation delay at the EMS. In (6)-(7), quantities:

$$\boldsymbol{\xi} = [\theta, \phi]^T = J\left(-\mathbf{Q}_z(\psi)\mathbf{x}\right) \tag{8}$$

$$\boldsymbol{\zeta} = [\widetilde{\theta}, \widetilde{\phi}]^T = J\left(\mathbf{x}\right) \tag{9}$$

denote, respectively, the incidence/reflection angles at the EMS and the transmission/reception pointing angles to/from the EMS at the sensing terminal. $J(\cdot)$ is a non-linear transformation between global Cartesian coordinates to EMS-local spherical coordinates, namely:

$$J(\mathbf{x}) : \begin{cases} \theta = \arctan\left(\dfrac{y}{x}\right), \\ \phi = \arccos\left(\dfrac{z}{\|\mathbf{x}\|}\right), \end{cases} \tag{10}$$

$$\begin{aligned} y_\ell(t) &= \rho \sum_{n,m} e^{-j2\pi f_0(\tau^i_{\ell,nm}+\tau^o_{\ell,nm})} e^{j\Phi_{nm}}\, s\left(t-\tau^i_{\ell,nm}-\tau^o_{\ell,nm}\right) + z_\ell(t) \\ &\overset{(a)}{\approx} \rho\, e^{-j4\pi f_0\tau_0} e^{-j2\pi f_0(\Delta\tau^i_\ell+\Delta\tau^o_\ell)} \sum_{n,m} e^{-j4\pi f_0\Delta\tau_{nm}(\boldsymbol{\xi})} e^{j\Phi_{nm}} s\left(t-2\tau_0-\Delta\tau^i_\ell-\Delta\tau^o_\ell-2\Delta\tau_{nm}(\boldsymbol{\xi})\right) + z_\ell(t), \end{aligned} \tag{4}$$

while

$$\mathbf{u}(\boldsymbol{\xi}) = [\sin\phi\cos\theta, \sin\phi\sin\theta, \cos\phi]^T \tag{11}$$

is a unit vector defining a direction in local or global coordinates. For the considered planar EMS, the residual propagation delay is expressed as:

$$\Delta\tau_{nm}(\boldsymbol{\xi}) = \frac{d}{c}\left[n\sin\phi\cos\theta + m\sin\phi\sin\theta\right]. \tag{12}$$

Under far-field assumption, the phase at the EMS can be configured according to a desired incidence/reflection angle $\overline{\boldsymbol{\xi}}$ at center bandwidth (f_0) as:

$$\Phi_{nm}(\overline{\boldsymbol{\xi}}) = \frac{4\pi f_0 d}{c}\left[n\sin\overline{\phi}\cos\overline{\theta} + m\sin\overline{\phi}\sin\overline{\theta}\right] \tag{13}$$

so as to compensate the propagation phase $4\pi f_0\Delta\tau_{nm}(\boldsymbol{\xi})$ and maximize the reflection gain at f_0 for $\overline{\boldsymbol{\xi}} = \boldsymbol{\xi}$. Model $(4)(a)$ is suitable for carrier-phase ranging, i.e., where the absolute propagation delay τ_0 can be estimated by exploiting the carrier phase term $e^{-j4\pi f_0\tau_0}$. This is markedly different from conventional localization systems that only use the baseband term $s(t-2\tau_0)$ (thus dropping $e^{-j4\pi f_0\tau_0}$ in $(4)(a)$), but carrier-phase ranging and localization allows achieving the utter performance [50], and it is therefore considered in this paper through the adoption of radio-frequency model $(4)(a)$.

B. System Model in Frequency Domain

When the bandwidth B of the Tx signal is large enough to induce spatial wideband effects at the EMS and/or at the sensing terminal, the reflection gain is maximized only around the carrier frequency f_0, and *beam squinting* effects arise. Spatial wideband effect is a well-known issue in radars [51], and in the considered system arises for

$$\left|\frac{d}{c}\sin\phi\left[N\cos\theta + M\sin\theta\right]\right| > \frac{1}{B} \tag{14}$$

i.e., when the residual propagation delay across the EMS is comparable (or larger) than the pulse duration after range compression. For normal incidence onto the metasurface ($\phi = 0$), the spatial wideband effect does not occur, regardless of B.

The system model $(4)(a)$, is conveniently written in the frequency domain by operating a Fourier transform over $y_\ell(t)$, obtaining

$$\begin{aligned} Y_\ell(f) &\overset{(a)}{\approx} S(f)\, e^{-j2\pi(f_0+f)(2\tau_0+\Delta\tau^i_\ell+\Delta\tau^o_\ell)} \\ &\times \underbrace{\rho \sum_{n,m} e^{-j4\pi(f_0+f)\Delta\tau_{nm}(\boldsymbol{\xi})} e^{j\Phi_{nm}(\overline{\boldsymbol{\xi}})}}_{\beta(f,\boldsymbol{\xi}|\overline{\boldsymbol{\xi}})} + Z_\ell(f) \end{aligned} \tag{15}$$

where f denotes the base-band frequency (i.e., around f_0), $\beta(f,\boldsymbol{\xi}|\overline{\boldsymbol{\xi}})$ is the frequency-dependent scattering amplitude term incorporating both the geometrical energy losses (ρ) and the reflection gain of the RIS, while $Z_\ell(f) \sim \mathcal{CN}(0, N_0\delta(f)\delta_{\ell-k})$ is the noise in frequency, with power spectral density N_0, uncorrelated across channels. The spatial narrowband operation of the EMS w.r.t. the impinging sensing signal, largely assumed in literature, is derived from (15) by plugging $e^{-j4\pi f_0\Delta\tau_{nm}(\boldsymbol{\xi})}$ in place of $e^{-j4\pi(f_0+f)\Delta\tau_{nm}(\boldsymbol{\xi})}$. This is equivalent to assert that $s(t-2\tau_0-2\Delta\tau_{nm}) \simeq s(t-2\tau_0)$ in $(4)(a)$. The model of $\beta(f,\boldsymbol{\xi}|\overline{\boldsymbol{\xi}})$ follows from the radar equation [52]:

$$\beta(f,\boldsymbol{\xi}|\overline{\boldsymbol{\xi}}) = \sqrt{\frac{c^2}{f_0^2(4\pi)^3\|\mathbf{x}\|^4}\Gamma_{\text{ris}}(f,\boldsymbol{\xi}|\overline{\boldsymbol{\xi}})}\; e^{j\gamma} \tag{16}$$

where the path-loss depends only on the distance from the phase center of the sensing terminal[1], $\Gamma_{\text{ris}}(f,\boldsymbol{\xi}|\overline{\boldsymbol{\xi}})$ is the RCS of the EMS and γ is a phase term modeling residual phase uncertainties about the target arising from Tx-Rx circuitry, Doppler effects from motion, etc. The RCS of the EMS is an implicit function of the EMS position $\mathbf{x}$ and angles $\boldsymbol{\xi}$.

IV. RIS-Based Reflector Design

Let us consider the usage of a RIS as a retro-reflector. The RIS behaves as a reconfigurable passive device, i.e., no amplification gain or other advanced processing is implemented at the RIS side [53]. The perfect phase configuration follows from (13) by plugging $\overline{\boldsymbol{\xi}} = \boldsymbol{\xi}$. In this latter setting, the sensing system experiences the maximum possible monostatic RCS of the RIS at f_0, that can be generally expressed as follows:

$$\Gamma_{\text{ris}}(f,\boldsymbol{\xi}|\overline{\boldsymbol{\xi}}) = \Gamma^{\max}_{\text{ris}}(f)\; G(f,\boldsymbol{\xi}|\overline{\boldsymbol{\xi}}) \tag{17}$$

where $\Gamma^{\max}_{\text{ris}}(f)$ is the peak monostatic RCS of the RIS, function of the base-band frequency f, while $G(f,\boldsymbol{\xi}|\overline{\boldsymbol{\xi}})$ is the normalized monostatic RCS of the RIS (array factor). The expression of $G(f,\boldsymbol{\xi}|\overline{\boldsymbol{\xi}})$ is:

$$\begin{aligned} G(f,\boldsymbol{\xi}|\overline{\boldsymbol{\xi}}) &= \left|\frac{1}{NM}\sum_{n,m} e^{-j4\pi(f_0+f)\Delta\tau_{nm}(\boldsymbol{\xi})} e^{j\Phi_{nm}(\overline{\boldsymbol{\xi}})}\right|^2 \\ &= \left|\frac{\sin\left(N\alpha_x(f,\boldsymbol{\xi}|\overline{\boldsymbol{\xi}})\right)}{N\sin\left(\alpha_x(f,\boldsymbol{\xi}|\overline{\boldsymbol{\xi}})\right)}\frac{\sin\left(M\alpha_y(f,\boldsymbol{\xi}|\overline{\boldsymbol{\xi}})\right)}{M\sin\left(\alpha_y(f,\boldsymbol{\xi}|\overline{\boldsymbol{\xi}})\right)}\right|^2 \end{aligned} \tag{18}$$

where

$$\alpha_x(f,\boldsymbol{\xi}|\overline{\boldsymbol{\xi}}) = \frac{2\pi d}{c}\left[f_0\sin\overline{\phi}\cos\overline{\theta} - (f_0+f)\sin\phi\cos\theta\right], \tag{19}$$

$$\alpha_y(f,\boldsymbol{\xi}|\overline{\boldsymbol{\xi}}) = \frac{2\pi d}{c}\left[f_0\sin\overline{\phi}\sin\overline{\theta} - (f_0+f)\sin\phi\sin\theta\right]. \tag{20}$$

For $\overline{\boldsymbol{\xi}} = \boldsymbol{\xi}$, the normalized monostatic RCS is ≤ 1 except for $f = 0$ (i.e., at center bandwidth f_0) due to the frequency-dependent squinting effects. The peak RCS can

[1]This approximation holds for monostatic setups where the size of the sensing arrays is much lower than the distance with targets.

be well approximated by the RCS of a metallic plate of area $A_{\text{ris}} = NMd^2$ perpendicular to the incidence/reflection direction as [54], [55]:

$$\Gamma_{\text{ris}}^{\max}(f) = \frac{4\pi f^2 A_{\text{ris}}^2}{c^2} = \frac{4\pi f^2 (NM)^2 d^4}{c^2} \quad [\text{m}^2]. \tag{21}$$

For a 10×10 cm^2 RIS operating at $f_0 = 77$ GHz frequency, the RCS@f_0 is 72.5 m^2, comparable with the one of a tetrahedral corner reflector of 10 cm for each side. The RIS size, namely the number of elements $N \times M$ shall be designed to achieve:

$$\Gamma_{\text{ris}}^{\max}(f_0) \geq \Gamma_{\min} \tag{22}$$

with $\Gamma_{\min}$ being a minimum RCS that ensures the detectability of the RIS. A rule of thumb, here proposed, is to compute it based on the ratio between the corner reflector's RCS and the maximum measured car's RCS. Based on the experimental radar measurements reported in Section II, we observed a ratio of 10 dB. The RCS of the corner reflector Γ_{CR} with side a is defined as [52]:

$$\Gamma_{\text{CR}}^{\max}(f_0) = \frac{12\pi f_0^2 a^4}{c^2}, \quad [\text{m}^2]. \tag{23}$$

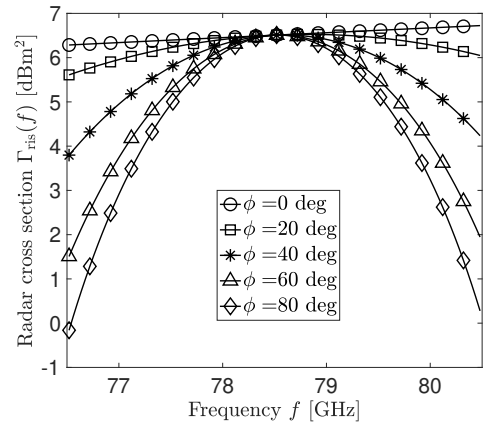

(a) $A_{\text{ris}} = 4.5 \times 4.5$ cm^2

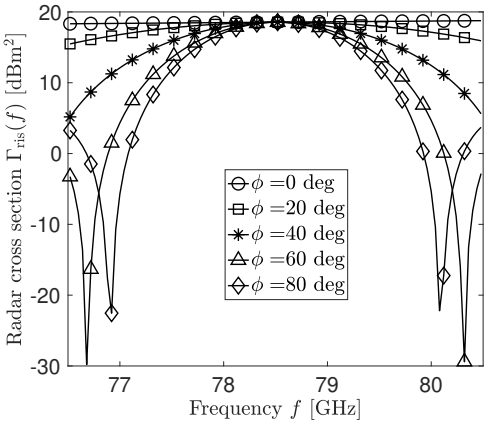

(b) $A_{\text{ris}} = 9.2 \times 9.2$ cm^2

Fig. 6: RCS of the RIS varying the incident signal frequency and elevation angle ϕ, for (6a) a $A_{\text{ris}} = 4.5 \times 4.5$ cm^2 RIS and (6b) a $A_{\text{ris}} = 9.2 \times 9.2$ cm^2 RIS.

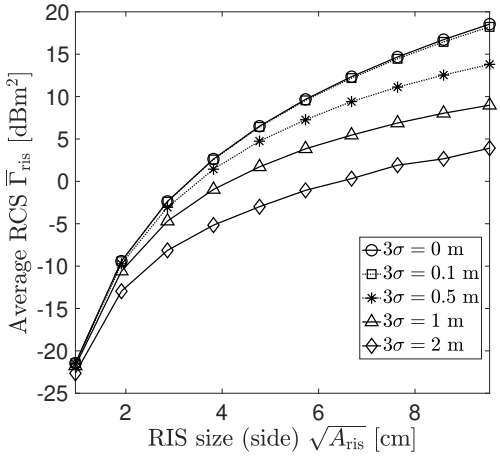

Fig. 7: Effect of positioning error on the experienced RCS: average RCS $\overline{\Gamma}_{\text{ris}}(\boldsymbol{\xi})$ (in dBm^2) as a function of the RIS size varying the positioning error σ.

The area of the RIS can be computed based on (21) and (23) as:

$$\Gamma_{\text{ris}}^{\max}(f_0) = \frac{\Gamma_{\text{CR}}^{\max}(f_0)}{10} \longrightarrow A_{\text{ris}} \approx a^2 \sqrt{\frac{3}{10}} \tag{24}$$

corresponding to a RIS with an area $A_{\text{ris}} = 7.4 \times 7.4$ cm^2. However, even in the ideal case of a perfect phase configuration, the reflection beam squinting cannot be ignored in the experienced RCS by a sensing system illuminating the RIS. The beam squinting follows from (18). Simplifying the geometry, by setting $\theta = \overline{\theta} = 0$, the elevation angle of maximum reflection is:

$$\phi_{peak}(f) = \arcsin\left(\frac{f_0}{f_0 + f} \sin\overline{\phi}\right) \tag{25}$$

By fixing the observation direction $\boldsymbol{\xi}$, the normalized monostatic RCS of the RIS as a function of the frequency f defines its frequency response for the impinging sensing signal. It can be demonstrated (but not reported for brevity) that only the elevation angle is affected by squinting. Fig. 6 shows the trend of the monostatic RCS $\Gamma_{\text{ris}}(f, \boldsymbol{\xi}|\boldsymbol{\xi})$ as function of the frequency, for $\theta = 0$ deg (azimuth) and $\phi = 0, 20, 40, 60, 80$ deg (elevation). It is immediate to notice that, for increasing grazing angles ϕ, the frequency-selectivity of the RIS increases as well, *filtering* the impinging signal. For a typical bandwidth $B = 4$ GHz, $\phi = 60$ deg, the RCS decreases by 4 dB for a 4.5×4.5 cm^2 RIS and by 30 dB for a 9.2×9.2 cm^2 RIS.

A. RIS Configuration in Realistic Settings

In practice, the vehicle does not have the perfect knowledge of the RIS pointing angles $\boldsymbol{\xi}$, and the RIS phase configuration leverages on suitable estimated angles $\widehat{\boldsymbol{\xi}}$. A typical source of error on $\boldsymbol{\xi}$ is the mobility of the vehicle w.r.t. the sensing terminal, which makes any estimated data $\widehat{\boldsymbol{\xi}}$ rapidly outdated. The phase pattern applied to the RIS reflector is:

$$\Phi_{nm}(\widehat{\boldsymbol{\xi}}) = \frac{4\pi f_0 d}{c}\left[n \sin\widehat{\phi}\cos\widehat{\theta} + m \sin\widehat{\phi}\sin\widehat{\theta}\right] \tag{26}$$

and the corresponding RCS experienced by the sensing system can be computed using (17) and plugging $\overline{\boldsymbol{\xi}} = \widehat{\boldsymbol{\xi}}$ in (18).

Notice that leveraging on-board positioning systems (e.g., GPS) is not generally sufficient to attain the desired localization performance as *(i)* the spatial resolution of sensing systems may be much higher than the positioning accuracy of current technologies[2] and *(ii)* the average experienced RCS is low. To gain insight into this latter aspect, let us consider the case in which the vehicle has a coarse estimate of the incidence/reflection angles:

$$\widehat{\boldsymbol{\xi}} = [\widehat{\theta}, \widehat{\phi}]^T = J\left(-\mathbf{Q}_z(\psi)\widehat{\mathbf{x}}\right) \tag{27}$$

where $\widehat{\mathbf{x}} \sim \mathcal{N}(\mathbf{x}, \mathbf{C}_{\mathbf{x}})$ is the on-board position measurement made by the vehicle, characterized by covariance $\mathbf{C}_{\mathbf{x}} = \sigma^2 \mathbf{I}_3$[3]. Figure 7 shows the trend of the average RCS $\overline{\Gamma}_{\text{ris}}(\boldsymbol{\xi})$ experienced by the sensing system varying the RIS size (assuming a squared RIS of $N \times N$ elements, spaced by $d = \lambda_0/4$ at $f_0 = 78.5$ GHz). The sensing terminal is in the origin of the reference system, at 6.5 m above the RIS, which is located in $\mathbf{x} = [10, 0, -6.5]^{\text{T}}$. The RIS position is known with variable accuracy $3\sigma = 0,\ 0.1,\ 0.5,\ 1,\ 2$ m, and the RIS phase is configured based on the estimated position $\widehat{\mathbf{x}}$ as $\Phi_{nm}(\widehat{\boldsymbol{\xi}})$. We observe a gap between the expected peak RCS $\Gamma_{\text{ris}}^{\max}(f)$ and the average one $\overline{\Gamma}_{\text{ris}}(f, \boldsymbol{\xi})$, that progressively increases with the RIS size and with localization uncertainty σ. The consequence of inaccurate estimation of $\widehat{\boldsymbol{\xi}}$ is that the RIS will not be configured optimally, resulting in a loss of the experienced RCS, which is more severe as the spatial selectivity of the RIS increases.

An effective solution to overcome the aforementioned issue is to refine the estimation of the RIS configuration angles $\boldsymbol{\xi}$ by a local search over the angular span defined by the confidence on the initial, coarse estimate $\widehat{\boldsymbol{\xi}}$. Let us define as $\mathbf{C}_{\boldsymbol{\xi}} = \mathbf{J}\mathbf{C}_{\mathbf{x}}\mathbf{J}^T \in \mathbb{R}^{2\times 2}$ the covariance matrix of the angular estimation error $\widehat{\boldsymbol{\xi}} - \boldsymbol{\xi}$, where $\mathbf{J} \in \mathbb{R}^{2\times 3}$ is the Jacobian matrix of the transformation $J(\cdot)$ in (10) evaluated in the estimated position $\widehat{\mathbf{x}}$. The optimal RIS configuration angles are obtained with the following *RIS alignment procedure*:

$$\boldsymbol{\xi}_{opt} = \underset{\boldsymbol{\xi}_{k,q} \in \Xi_{\text{ris}}}{\operatorname{argmax}}\ \Gamma_{\text{ris}}(f_0, \boldsymbol{\xi}_{k,q} | \boldsymbol{\xi}) \tag{28}$$

where $\Gamma_{\text{ris}}(f_0, \boldsymbol{\xi}_{k,q}|\boldsymbol{\xi})$ is the RCS at f_0 experienced by choosing the reflection angles $\boldsymbol{\xi}_{k,q} = [\theta_k, \phi_q]^T$ within the finite set $\Xi_{\text{ris}} = \Theta_{\text{ris}} \times \Psi_{\text{ris}}$. Then, the optimal configuration of the RIS is $\Phi_{nm}(\boldsymbol{\xi}_{opt}) \simeq \Phi_{nm}(\boldsymbol{\xi})$. Set Ξ_{ris} is *dynamically* updated based on the estimated angles $\widehat{\boldsymbol{\xi}}$ and the related uncertainties $\sigma_\theta = \sqrt{[\mathbf{C}_{\boldsymbol{\xi}}]_{(1,1)}}$ and $\sigma_\phi = \sqrt{[\mathbf{C}_{\boldsymbol{\xi}}]_{(2,2)}}$, as

$$\Theta_{\text{ris}} = \left\{ \theta_k \,\middle|\, \theta_k = \widehat{\theta} + k\left(\frac{\Delta\theta}{\kappa\sigma_\theta}\right), k = -\frac{K}{2}, \ldots \frac{K}{2} \right\} \tag{29}$$

$$\Psi_{\text{ris}} = \left\{ \phi_q \,\middle|\, \phi_q = \widehat{\phi} + q\left(\frac{\Delta\phi}{\kappa\sigma_\phi}\right), q = -\frac{Q}{2}, \ldots \frac{Q}{2} \right\} \tag{30}$$

where: *(i)* $\Delta\theta$ and $\Delta\phi$ are the reflection beamwidths in azimuth and elevation, *(ii)* $K = \lceil 2\kappa\sigma_\theta/\Delta\theta \rfloor$ and $Q = \lceil 2\kappa\sigma_\phi/\Delta\phi \rfloor$ are the codebooks' cardinalities, and *(iii)* $\kappa \geq 1$ is a proper factor accounting for a pre-defined confidence interval, e.g., $\kappa = 3$. Sets Θ_{ris} and Ψ_{ris} denote the spanned azimuth and elevation angles, respectively, within a given confidence. The proposed method converges to the optimal value of configuration angles, with a residual error that depends on the codebook cardinality. In practice, the RIS alignment procedure requires dedicated control signaling from the sensing terminal to the vehicle to *(i)* share the position of the sensing terminal, *(ii)* synchronize the reflection sweeping time with the PRI of the sensing terminal, T_{PRI}, and *(iii)* communicate the optimal reflection beam to the vehicle once the procedure is finished. In the following, we provide some considerations on the RIS alignment procedure related to mobility.

B. Mobility Considerations

The duration of the RIS alignment procedure in mobility must ensure that the optimal RIS configuration $\boldsymbol{\xi}_{opt} = \boldsymbol{\xi}$ does not change within the interval T_{align}. We can evaluate the maximum alignment time by assuming a vehicle moving at velocity v in the coverage area of the sensing system. If the RIS-equipped vehicle crosses the boresight of the sensing terminal at distance $D_{\min}$, the alignment time shall be limited by:

$$v\, T_{\text{align,az}} \leq \Delta\theta D_{\min} \tag{31}$$

where $\Delta\theta D_{\min}$ is the projection of the azimuth reflection beamwidth at the sensing terminal side. The reasoning is simple: the space travelled by the vehicle shall be within the projected reflection beam. Similarly, if the vehicle is moving away from the sensing terminal, we have a similar inequality for elevation as:

$$v\, T_{\text{align,el}} \leq \frac{\Delta\phi D_{\min}}{\cos\phi_{\min}} \tag{32}$$

where $\Delta\phi D_{\min}/\cos\phi_{\min}$ is the projection of the elevation reflection beamwidth at the sensing terminal side. Thus, a conservative upper-bound for the alignment time is obtained by:

$$T_{\text{align}} = T_{\text{PRI}} \min\left(\underbrace{\frac{\Delta\theta D_{\min}}{vT_{\text{PRI}}}}_{K_{\max}}, \underbrace{\frac{\Delta\phi D_{\min}}{vT_{\text{PRI}}\cos\phi_{\min}}}_{Q_{\max}} \right) \tag{33}$$

where we expressed the alignment time as a multiple of the fundamental unit of time of the sensing system T_{PRI}, used to test a single reflection beam. Quantity T_{PRI} does not depend on the RIS switching capability, but rather can be well approximated by the pulse repetition interval (PRI) of the sensing system (tens of μs [56]). The second term is the minimum between the maximum number of reflection beams that can be tested along azimuth and elevation, evaluated at the minimum distance from the sensing terminal. Notice that the design of the RIS-alignment procedure does not need to explicitly take into account the Doppler shift of the vehicle in (33), as the mobility is described by velocity v. In fact,

[2]A typical GPS has a positioning accuracy in the order of 1 m to few m (without urban canyoning effects), while a MIMO radar working at $f_0 =$ 77 GHz with 25 cm of aperture ($\approx$ 100 *virtual* antennas) and 3 GHz of bandwidth (e.g., [56]) has a resolution cell of 15×5 cm at 20 m distance, comparable with the one of an expensive RTK setup

[3]The choice of a circular Gaussian error model, as well as a diagonal covariance matrix, is dictated by the seek for simplicity in the numerical derivations herein, but does not limit the validity of the results.

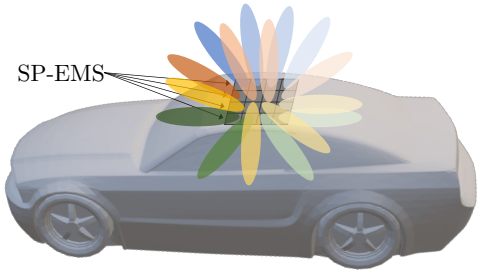

Fig. 8: SP-EMSs on the roof of the vehicle for omnidirectional localization. Different colors denote retro-reflection from different modules.

Doppler shift does not affect the received signal power as for (15).

Example: Considering a typical urban scenario, where $v = 50$ km/h, a typical PRI $T_{\text{PRI}} = 50$ μs, $f_0 = 77$ GHz, $D_{\min} = 10$ m ($\phi_{\min} = 45$ deg), and $Nd = 10$ cm ($\Delta\theta = 0.5$ deg, $\Delta\phi = 2.5$ deg) we have that $K_{\max} \simeq 125$ and $Q_{\max} \simeq 900$, thus it is dominated by the azimuth sweeping procedure. For a positioning uncertainty of $3\sigma = 2$ m (along x, y and z, i.e., circular), we have that the number of beams that must be tested by the sensing system is $\frac{3\sigma}{\Delta\theta D_{\min}} \simeq 22 \ll K_{\max}$ (azimuth) and $\frac{3\sigma\cos\phi_{\min}}{\Delta\phi D_{\min}} \simeq 4 \ll Q_{\max}$ (elevation), which are far below the limit imposed by (33). In highway scenarios with $v = 150$ km/h, the PRI of the system must be reduced for non-ambiguous Doppler estimation (see [57]), e.g., $T_{\text{PRI}} \leq 30$ μs, thus $K_{\max} \simeq 70$, $Q_{\max} \simeq 500$, still above the number of beams to be tested dictated by (33).

V. SP-EMS-based Reflector Design

A cost-effective alternative to RIS-based reflectors, considered hereinafter, consists of a fully passive and static retro-reflector, belonging to the class of SP-EMSs [41]–[43]. Since the wave manipulation capabilities of an SP-EMS are defined in the design phase, the maximum retro-reflection can be guaranteed only toward the designated direction. Hence, a suitable solution is to have multiple SP-EMSs, hereafter referred to as *modules*, composing an omnidirectional retro-reflector, whereby each module is differently configured to retro-reflect the impinging signal from a specific direction, as indicated in Fig. 8. To this aim, consider the case of having P modules. The location of the (n,m)-th meta-atom of the p-th module is therefore:

$$\mathbf{x}_{p,nm} = \mathbf{x}_p + \mathbf{Q}_z(\psi)\mathbf{p}_{nm}, \tag{34}$$

where $\mathbf{x}_p = \mathbf{x} + \mathbf{p}_p$ is the location of the p-th module in global coordinates ($\mathbf{p}_p$ is the position in local coordinates). The p-th module is configured to retro-reflect the impinging signal from direction $\overline{\boldsymbol{\xi}}_p = [\cos\overline{\theta}_p, \sin\overline{\phi}_p]^T$:

$$\Phi_{nm}(\overline{\boldsymbol{\xi}}_p) = \frac{4\pi f_0 d}{c}\left[n\sin\overline{\phi}_p\cos\overline{\theta}_p + m\sin\overline{\phi}_p\sin\overline{\theta}_p\right]. \tag{35}$$

The monostatic RCS of the SP-EMS, accounting for *all* the modules, is evaluated as in (36), where $\Gamma_{\text{mod}}^{\max}(f)$ is the frequency-dependent peak monostatic RCS of the single module, while $G(f,\boldsymbol{\xi}|\{\overline{\boldsymbol{\xi}}_p\}_{p=1}^P)$ is the monostatic reflection pattern of the SP-EMS. The set of modules composing the SP-EMS can be designed such that: (1) the minimum RCS of each module is sufficient to make it detectable in the sensing image, (2) the retro-reflection main lobe of each module is well separated to the others in the angular domain, i.e., for a specific incidence direction $\overline{\boldsymbol{\xi}}$, only one module will effectively contribute to the retro-reflection and (3) each module must work over the whole sensing bandwidth, with no or limited filtering of the impinging signal (see Section IV). Criterion (1) follows from the empirical method derived in Section IV, (24), providing module sizes ranging from 4×4 cm^2 to 10×10 cm^2. Criterion (2) provides a guideline for the design of single modules, such that to achieve the full angular coverage (azimuth and elevation), namely guaranteeing that the SP-EMS back-reflects a sufficient amount of energy when illuminated by any direction. For a first-order evaluation of the monostatic RCS of the SP-EMS, we can approximate the reflection pattern (normalized monostatic RCS) as[4]:

$$G(f,\boldsymbol{\xi}|\{\overline{\boldsymbol{\xi}}_p\}_{p=1}^P) \approx G(f,\boldsymbol{\xi}|\overline{\boldsymbol{\xi}}_{\overline{p}}) = \frac{1}{(NM)^2}\sum_{n,m} e^{-j4\pi(f_0+f)\Delta\tau_{nm}(\boldsymbol{\xi})} e^{j\Phi_{nm}(\overline{\boldsymbol{\xi}}_{\overline{p}})} \tag{37}$$

i.e., dominated by a single module, whose configuration angle $\overline{\boldsymbol{\xi}}_{\overline{p}}$ is the closest to the true direction of observation $\boldsymbol{\xi}$, $\overline{p} = \text{argmin}_p\left\{\|\boldsymbol{\xi} - \overline{\boldsymbol{\xi}}_p\|^2\right\}$. Criterion (3) constraints the design of the SP-EMS reflector, which shall trade between reflectivity (large modules) and robustness to frequency selectivity (i.e., spatial wideband effects, small modules).

A. Design of the SP-EMS, Full-Wave Modeling, and Manufacturing Options

The design of SP-EMS has been widely discussed in the recent literature on the topic, with several examples already

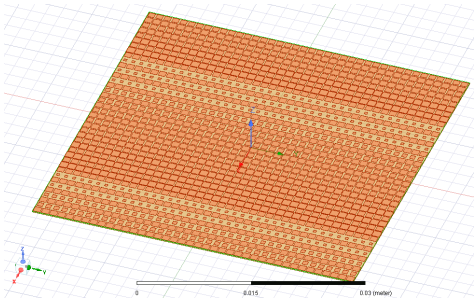

Fig. 9: SP-EMS module in HFSS

[4]The approximation by (37) is a lower bound on the monostatic RCS, i.e., for $\boldsymbol{\xi}_i = \boldsymbol{\xi}_o = \boldsymbol{\xi}$. The presence of multiple modules with different configuration angles $\{\overline{\boldsymbol{\xi}}_p\}$ generate additional reflection peaks at $\boldsymbol{\xi}_i \neq \boldsymbol{\xi}_o$ (that can be computed from the generalized Snell's law). For example, considering two modules configured to back-reflect at $\overline{\phi}_1 = 30$ deg and $\overline{\phi}_2 = 40$ deg, by illuminating the SP-EMS at $\phi_i = 30$ deg we obtain two peaks: $\phi_o = \overline{\phi}_1 + (\overline{\phi}_1 - \phi_i) = 30$ deg (retro-reflection) and $\phi_o = \overline{\phi}_2 + (\overline{\phi}_2 - \phi_i) = 50$ deg. When the number of modules increases, additional reflection peaks can be aligned with the impinging direction, increasing the monostatic RCS.

$$\Gamma_{\mathrm{EMS}}(f,\boldsymbol{\xi}|\{\bar{\boldsymbol{\xi}}_p\}_{p=1}^{P}) = \Gamma_{\mathrm{mod}}^{\max}(f)\underbrace{\sum_{p=1}^{P}\frac{1}{(NM)^2}\sum_{n,m}e^{-j4\pi(f_0+f)\Delta\tau_{nm}(\boldsymbol{\xi})}e^{j\Phi_{nm}(\bar{\boldsymbol{\xi}}_p)}}_{G(f,\boldsymbol{\xi}|\{\bar{\boldsymbol{\xi}}_p\}_{p=1}^{P})} \tag{36}$$

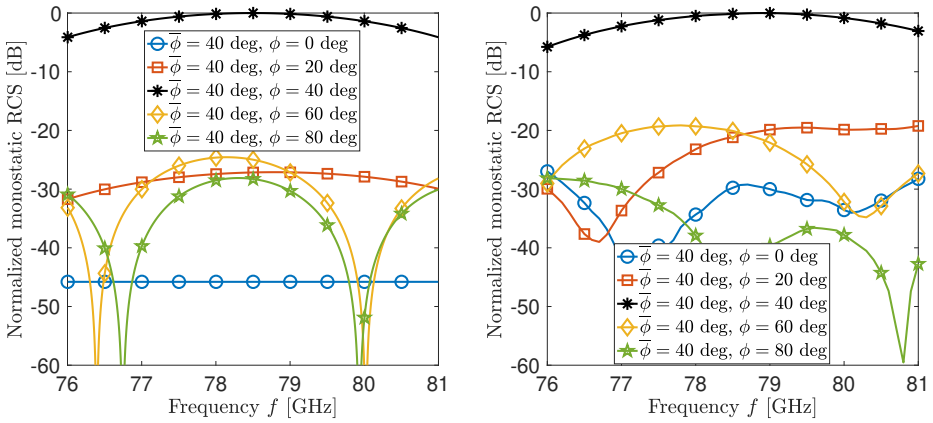

(a) SP-EMS size 4.58×4.58 cm^2 (analytical model (18))

(b) SP-EMS size 4.58×4.58 cm^2 (HFSS)

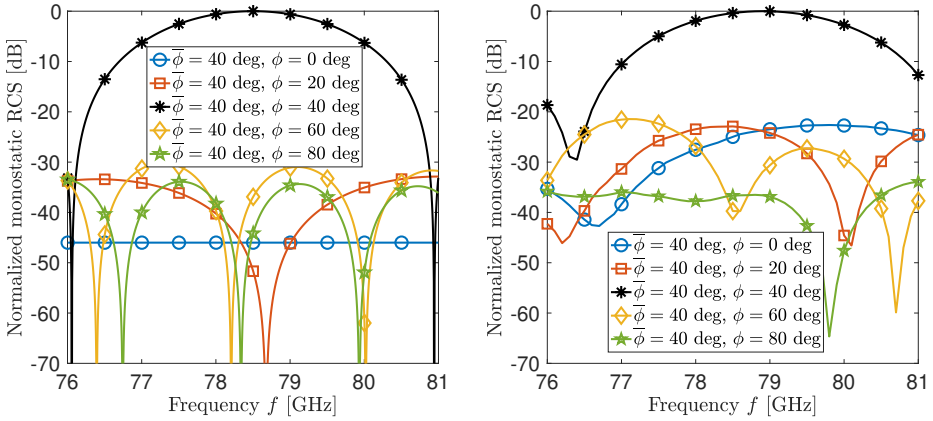

(c) SP-EMS size 9.17×9.17 cm^2 (analytical model (18))

(d) SP-EMS size 9.17×9.17 cm^2 (HFSS)

Fig. 10: Normalized monostatic RCS of the single SP-EMS module according to (a,c) the analytical model (18) and (b,d) Ansys HFSS, for (a,b) a 4.58×4.58 cm^2 SP-EMS size (c,d) 9.17×9.17 cm^2 SP-EMS size. The design process has been carried out assuming a central frequency of $f_0 = 78.5$ GHz and combining $\lambda_0/3$-spaced meta-atoms printed on a Rogers3003 substrate. In all cases, the SP-EMS is configured to retro-reflect the incident signal from $\bar{\boldsymbol{\xi}} = [\bar{\theta}, \bar{\phi}]^T = [0, 40]^T$ deg according to the generalized Snell's law.

demonstrated in smart environment applications [41]–[43]. In the following, this concept is customized to the design of retro-reflecting planar structures according to the following guidelines: *(i)* the meta-atomic structure is chosen to comply with a sub-wavelength lattice (i.e., $0.3\lambda_0$ periodicity) to enable retro-reflection capability even for grazing angles ($\phi \to 90$ deg) as well as to enable proper homogenization tools to be adopted (based on the generalized sheet transition condition [41]–[43]); *(ii)* a ROGERS3003 substrate is chosen as a reference for the implementation of the meta-atom to guarantee an adequate trade-off between costs, losses, and overall efficiency in the considered bands; *(iii)* an elementary meta-atomic structure based on square printed patch with variable side is implemented to demonstrate that the conceived application does not require advanced multi-layer architectures or complex patterning schemes [41]–[43].

Following such considerations, the design of a set of SP-EMSs has been carried out through the system-by-design approach outlined in [41]–[43]. To this end, the meta-atom response has been firstly modeled in Ansys HFSS assuming local periodicity conditions to deduce the equivalent susceptibility tensors [41]–[43]. The design process has been then performed to implement the a-periodic SP-EMS patterning by assuming a retro-reflection according to the generalized Snell's law [41]–[43].

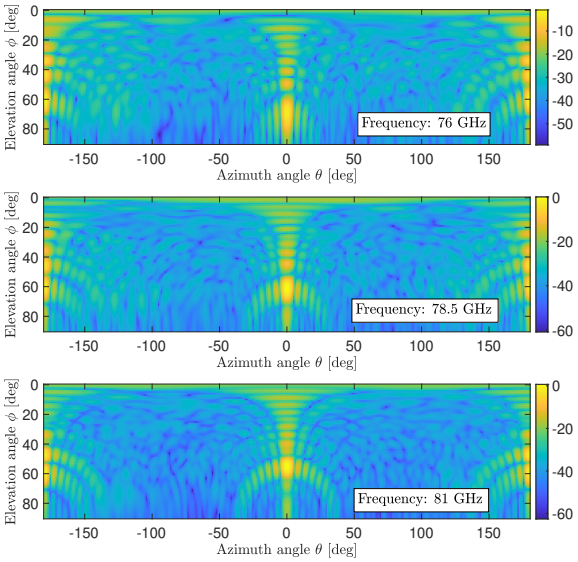

Fig. 11: Normalized bistatic RCS of a 4.58×4.58 cm^2 SP-EMS when illuminated from a fixed direction $\boldsymbol{\xi}_i = [\theta, \phi]^T = [0, 60]^T$ deg and phase-configured to retro-reflect at angles $\overline{\boldsymbol{\xi}} = [\overline{\theta}, \overline{\phi}]^T = [0, 60]^T$ deg. The RCS is evaluated for all the observation angles $\boldsymbol{\xi}_o$.

The full-wave results of the designed finite SP-EMSs obtained using Ansys HFSS are shown in Figs 10 and 11. Here, a plane wave illumination has been enforced, and the patterned structure has been modeled assuming a finite element-boundary integral (FE-BI) formulation to account for the edge effects and diffraction properties.

In Fig. 10, we show the normalized monostatic RCS for a single SP-EMS module of size 4.58×4.58 cm^2 (Figs. 10a and 10b) and 9.17×9.17 cm^2 (Figs. 10c and 10d), as function of the baseband frequency $f \in [76, 81]$ GHz. The module is configured to retro-reflect at $\overline{\boldsymbol{\xi}} = [\overline{\theta}, \overline{\phi}]^T = [0, 40]^T$ deg and it is tested at different angles $\boldsymbol{\xi} = [\theta, \phi]^T$ (incident and reflection). We let vary the elevation angle only (ϕ) by fixing the azimuth angle to $\theta = 0$ deg, such that to observe the reflection beam squinting effect in the frequency response of the SP-EMS module. We compare the results obtained with the analytical model for normalized monostatic RCS in (18) (Figs. 10a and 10c) with the Ansys HFSS results (Figs. 10b and 10d). We observe that the analytical model (18) allows having a closed-form description of the SP-EMS (or RIS) frequency response that is valid only around $\overline{\boldsymbol{\xi}} \simeq \boldsymbol{\xi}$ (i.e., it accurately describes the frequency response of the SP-EMS/RIS only within the main lobe of the reflection pattern). This can be concluded by comparing black curves in Figs. 10a and 10c with the black curves in Figs. 10b and 10d; the match is within few dBs of difference around the center frequency $f_0 = 78.5$ GHz. For $\phi \neq \overline{\phi}$ instead (colored curves), the difference is more pronounced, as Ansys HFSS provides accurate physical modeling of the SP-EMS that analytical models cannot capture. However, the observed order of magnitude of the RCS is similar.

Fig. 11, instead, shows the normalized *bistatic* RCS of a SP-EMS module of 4.58×4.58 cm^2 size, configured to retro-reflect at $\overline{\boldsymbol{\xi}} = [\overline{\theta}, \overline{\phi}]^T = [0, 60]^T$ deg. The bistatic RCS is obtained by illuminating the SP-EMS module with a plane wave from $\boldsymbol{\xi}_i = \overline{\boldsymbol{\xi}} = [0, 60]^T$ deg and evaluating the magnitude of the scattered magnitude electric field (squared) for arbitrary observation direction $\boldsymbol{\xi}_o$. The elevation angle of maximum reflection (i.e., the angular index of maximum bistatic RCS in Fig. 11) shifts from $\phi_{peak} = 70$ deg ($f = 76$ GHz) to $\phi_{peak} = 56$ deg ($f = 81$ GHz), while the azimuth does not change, as can be demonstrated. A similar trend is observed for the reflection beamwidth: at $f = 76$ GHz, the elevation beamwidth is $\Delta\phi = 20$ deg, while at $f = 81$ GHz it narrows to $\Delta\phi = 11$ deg (at $f_0 = 78.5$ GHz it amounts to $\Delta\phi = 15$ deg). In all cases, we have $\Delta\theta = 10$ deg. For the selected module size, the angle of peak reflectivity ϕ_{peak} falls within the -3 dB reflection beamwidth $\Delta\phi \; \forall f \in [76, 81]$ GHz, guaranteeing that the SP-EMS module is capable of retro-reflecting the signal without significant frequency-dependent power loss. With single modules of 4.58×4.58 cm^2 size and center bandwidth reflection beamwidth of $\Delta\theta = 10$ deg, $\Delta\phi = 15$ deg, we roughly need $36 \times 6 = 216$ modules to implement an omnidirectional retro-reflector, thus a composite SP-EMS of 60 cm side. Differently, employing modules of a larger size to increase its RCS, e.g., 9.17×9.17 cm^2, implies having a much larger footprint (the single module is larger and it also provides a narrower reflection beamwidth).

VI. Localization Performance

This section shows numerical results quantifying the localization performance bounds when the vehicle is equipped with an RIS. The same results would apply to the SP-EMS case; we refer to RIS for simplicity. To this aim, we evaluate the CRB on carrier-phase-based RIS's position estimation in the following cases: *(i)* perfect RIS configuration, i.e., the configuration angles $\overline{\boldsymbol{\xi}}$ are known and shall not be estimated and *(ii)* imperfect RIS configuration, i.e., the configuration angles $\overline{\boldsymbol{\xi}}$ are part of the parameters to be estimated. The CRB is evaluated in both spatial wideband and narrowband modeling assumptions, whereas narrowband is reported as a benchmark and it assumes:

$$s\left(t - 2\tau_0 - \Delta\tau_\ell^i - \Delta\tau_\ell^o - 2\Delta\tau_{nm}\right) \approx s\left(t - 2\tau_0\right) \tag{38}$$

in (4). Furthermore, to model the a-priori knowledge on the RIS position, that affects its configuration angles, we compute the HCRB for deterministic position $\mathbf{x}$ and random configuration angles $\overline{\boldsymbol{\xi}}$, characterized by distribution $p(\overline{\boldsymbol{\xi}}) = p(\widehat{\boldsymbol{\xi}})$. Details on CRB and HCRB derivations are reported in Appendix A. The employed metric is the position error bound (PEB), defined as:

$$\text{PEB} = \sqrt{\frac{\text{trace}\left([\mathbf{C}]_{1:3,1:3}\right)}{3}} \tag{39}$$

where $\mathbf{C}$ is either $\mathbf{C}_{\text{HCRB}}$ (for HCRB), $\mathbf{C}_{\text{CRB}}$ (for CRB) or $\mathbf{C}^{\text{u}}_{\text{CRB}}$ (for CRB and perfect RIS configuration). As a performance benchmark, we also show the PEB achieved without the usage of a dedicated EMS (RIS or SP-EMS). This PEB is obtained with the empirical criterion described

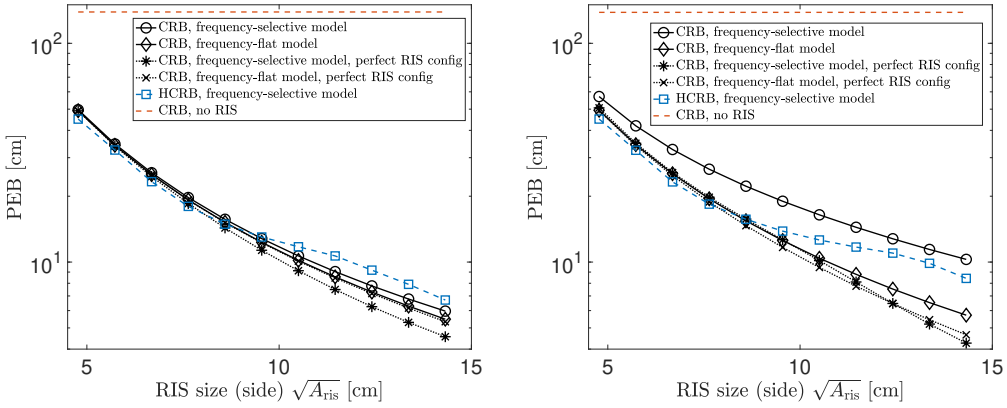

(a) $3\sigma = 0.5$ m, $B = 1$ GHz (b) $3\sigma = 0.5$ m, $B = 4$ GHz

(c) $3\sigma = 2$ m, $B = 1$ GHz (d) $3\sigma = 2$ m, $B = 4$ GHz

Fig. 12: PEB vs. RIS size for (a) $3\sigma = 0.5$ m, $B = 1$ GHz, (b) $3\sigma = 0.5$ m, $B = 4$ GHz, (c) $3\sigma = 2$ m, $B = 1$ GHz, (d) $3\sigma = 2$ m, $B = 4$ GHz.

by (24) (Section IV). We consider that the experienced RCS of the bare vehicle is at least 10 dB less w.r.t. the one of a RIS of 7.5×7.5 cm^2 size. Moreover, we take into account the fact that the strongest back-scattering point on the vehicle does not coincide with the desired location of the RIS on the roof, due to perspective deformations. This latter effect has been simulated with RemCom Wavefarer software [58] and acts a *bias* on the position estimate.

A. Simulation Parameters

Concerning simulation parameters, we consider the sensing terminal operating at $f_0 = 78.5$ GHz, on a variable bandwidth $B \in [1, 8]$ GHz, equipped with 1 Tx antenna and 20×20 Rx antennas along y and z axes. The RIS is made by $N = M = \sqrt{A_{\text{ris}}/d^2} \in [50, 150]$ elements at $\lambda_0/4$, corresponding to a size ranging from 4.7 cm to 14.3 cm. For the evaluation of the HCRB, we assume an a-priori knowledge of the configuration angles $\overline{\boldsymbol{\xi}}$ coming from a GPS-aided position estimation with uncertainty $3\sigma = 0.5$ m (as for an accurate RTK setup) and $3\sigma = 2$ m, as for an off-the-shelf GPS without urban canyoning effects. The RIS position $\mathbf{x}$ is instead treated as a deterministic parameter. The

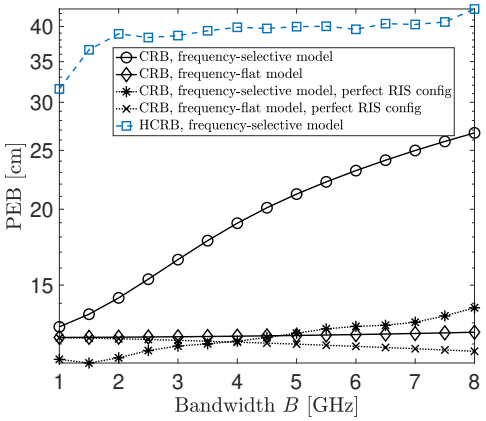

Fig. 13: PEB vs. bandwidth B for a 9.5×9.5 cm^2 RIS, carrier-phase localization.

sensing terminal is located in the origin of the reference system and the RIS in $\mathbf{x} = [10, 5, -6.5]^T$ m, which is a random position within the sensing coverage area. In all the following evaluations (except where differently indicated), the average power emitted by the sensing terminal is fixed and equal to

23 dBm (for each measurement channel, corresponding to an energy $E = 10^{-6}$ J over a time duration of $T = 50\mu$s), thus the power spectral density reduced with increasing B. The Rx signal is corrupted by thermal noise, $N_0 = -173$ dBm/Hz.

B. Performance Varying the RIS Size

The first set of results is summarized in Fig. 12. Here, we report both the HCRB and the CRB performance varying the RIS side $\sqrt{A_{\rm ris}}$. We also show the CRB of the narrowband model, namely assuming $\Gamma_{\rm ris}(f_0, \boldsymbol{\xi}|\overline{\boldsymbol{\xi}})$, no frequency selectivity of the reflection coefficient β. This is the commonly assumed framework in most of the available literature (e.g., see [11], [25]). Let us focus on the case $3\sigma = 0.5$ m, depicted in Figs. 12a and 12b for $B = 1$ GHz and $B = 4$ GHz, respectively. In the first case, the PEB provided by the CRB changes its behavior according to the knowledge (or not) of the configuration angles of the RIS $\overline{\boldsymbol{\xi}}$. For unknown (but deterministic) $\overline{\boldsymbol{\xi}}$ (solid black lines), the PEB of the narrowband model is lower than the PEB of the spatial wideband one. This is expected, as no spatial wideband modeling implies no filtering effects on the Tx signal due to the RIS (see Section IV-A) and therefore a higher Rx power. Differently, for $\overline{\boldsymbol{\xi}} = \boldsymbol{\xi}$ (perfect knowledge, dotted black lines), the PEB of the narrowband model is *higher* than the PEB of the spatial wideband one. In this latter case, when the phase of the RIS does not need to be estimated, (e.g., after the RIS alignment procedure as detailed in Section IV-A), the *position-dependent* frequency response of the sensing channel (via $\Gamma_{\rm ris}(f, \boldsymbol{\xi}|\overline{\boldsymbol{\xi}})$) introduces a non-negligible amount of information that allows compensating for the loss of Rx power due to the low-pass nature of $\Gamma_{\rm ris}(f, \boldsymbol{\xi}|\overline{\boldsymbol{\xi}})$. This effect is peculiar to a sensing system observing a RIS-equipped target and can be observed for $B = 1$ GHz (Fig. 12a) and also for $B = 4$ GHz (Fig. 12b), where, however, the filtering effect is stronger. Differently, the PEB provided by the HCRB (dashed blue curves) can be tighter than the PEB provided by CRB when the a-priori information is significant, as for $3\sigma = 0.5$ m. For higher inaccuracy on the angle estimation ($3\sigma = 2$ m, Figs. 12c and 12c) only the HCRB is affected, as expected. In general, HCRB provides a more conservative bound that better represents the case where one or more parameters are inherently random, as for $\overline{\boldsymbol{\xi}}$. In any case, we notice that the usage of an EMS consistently improves the localization performance compared to the bare vehicle case. The red dashed curve in Fig. 12, representing the performance we can expect without the RIS/SP-EMS, always exhibits the highest PEB.

C. Performance Varying the Employed Bandwidth

The trend of the PEB varying the employed bandwidth B is instead reported in Fig. 13, for $N = M = \sqrt{A_{\rm ris}/d^2} = 100$ (thus a 9.5×9.5 cm^2 RIS) and $3\sigma = 2$ m. The PEB by CRB for frequency-dependent RCS $\Gamma_{\rm ris}(f, \boldsymbol{\xi}|\overline{\boldsymbol{\xi}})$ monotonically increases with B. The former effect is the immediate consequence of the low-pass filtering of $\Gamma_{\rm ris}(f, \boldsymbol{\xi}|\overline{\boldsymbol{\xi}})$ on the incident signal, which reduces the retro-reflected energy in the direction of the sensing terminal. Differently, for narrowband system modeling, the PEB does not appreciably decrease with B. This

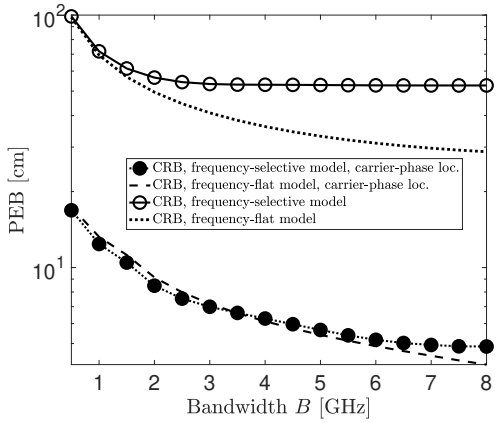

Fig. 14: PEB vs. bandwidth B for a 9.5×9.5 cm^2 RIS, comparing carrier-phase PEB and conventional PEB at fixed power spectral density of 32 dBm/GHz.

effect is typical of carrier-phase positioning systems (e.g., see [59]), and it is due to the effective bandwidth of the pass-band Tx signal (1), that is [60]:

$$B_{\rm eff}^2 = f_0^2 + \frac{B^2}{12} \approx f_0^2, \tag{40}$$

largely dominated by the carrier component for the considered settings, and almost insensitive to B (for $B = 10$ GHz and $f_0 = 77$ GHz, the first term of (40) is 3 orders of magnitude higher than the second). For $\overline{\boldsymbol{\xi}} = \boldsymbol{\xi}$ (perfect RIS configuration), instead, the spatial wideband model again provides an increasing PEB with B, that however, for $B \leq 3$ GHz, outperforms the narrowband model. This is the effect observed in Fig. 12. For $B > 3$ GHz, however, the information brought to the sensing system by the position-dependent frequency pattern of $\Gamma_{\rm ris}(f, \boldsymbol{\xi}|\overline{\boldsymbol{\xi}})$ is not sufficient to compensate for the severe power loss and the trend swaps. The HCRB, instead, increases for $B \leq 2$ GHz, but for larger values, the bandwidth B plays no significant role, as the PEB is approximately dominated by the uncertainty on $\overline{\boldsymbol{\xi}}$.

A further result stressing the importance of modeling the RIS's frequency response is provided in Fig. 14. It shows the PEB varying the bandwidth B for a 9.5×9.5 cm^2 RIS, with perfect phase configuration. We consider that the sensing terminal operates at fixed power spectral density, from 23 dBm at $B = 1$ GHz to 32 dBm at $B = 8$ GHz, yielding a decreasing PEB with increasing B. We compare the PEB for two models, namely *(i)* carrier-phase localization, described by (15), and *(ii)* conventional localization, whose model is obtained from (15) with the following substitution

$$e^{-j2\pi(f_0+f)(2\tau_0+\Delta\tau_\ell^i+\Delta\tau_\ell^o)} \rightarrow e^{-j4\pi f\tau_0} e^{-j2\pi(f_0+f)(\Delta\tau_\ell^i+\Delta\tau_\ell^o)}, \tag{41}$$

namely assuming that the absolute propagation delay τ_0 can be inferred by processing the base-band waveform only (and it is therefore proportional to the base-band frequency f, not f_0). The effective bandwidth of the system is therefore the one of the base-band signal $s(t)$, $B_{\rm eff}^2 = (\pi^2/3)B^2$. Carrier-phase PEB exhibits the same trend observed in Fig. 13, with an

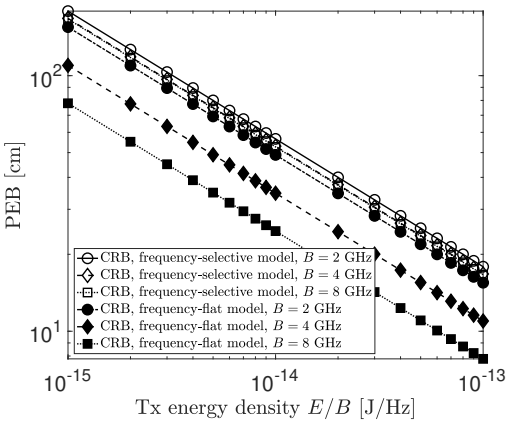

Fig. 15: PEB vs. energy spectral density for a 9.5×9.5 cm^2 RIS, comparing different bandwidth values.

improved PEB for $B \leq 3$ GHz and reduced performance for $B > 3$ GHz. Differently, a conventional localization approach leveraging the base-band waveform suffers a severe energy reduction due to RIS filtering, with no benefits. While the narrowband RIS model predicts a monotonic decrease of the PEB with B, the spatial wideband one yields a saturation value that depends on the specific low-pass frequency response of the RIS, depending on the RIS size and incidence elevation angle ϕ.

D. Performance Varying the Tx Energy

The last result concerns the trend of the PEB with the Tx energy. To this aim, Fig. 15 shows the PEB varying the Tx energy spectral density E/B for a 9.5×9.5 cm^2 RIS, with perfect phase configuration and $B = 2, 4, 8$ GHz. Conventional localization, as per (41), is considered, while the energy spectral density is such that the Tx average power on the PRI ranges from 20 to 40 dBm at $B = 4$ GHz. The PEB for the frequency-selective (wideband) RIS modeling is generally higher that the frequency-flat (narrowband) counterpart, due to the low-pass frequency response of the RIS over the different bandwidths. Moreover, the latter PEB gap increases with B, and it is insensitive to the employed Tx energy.

VII. Conclusion

This paper proposes lodging EMSs on vehicle roofs to increase their radar visibility and to make extended targets behave as point targets, easing their detection and tracking from sensing data. EMSs act as EM markers for impinging sensing signals, enabling intentional retro-reflections towards the sensing terminal (e.g., ISAC BS or MIMO radar). We detail the design of an RIS-based reflector considering the spatial wideband effect, that produces an in-band filtering on the impinging sensing signal, and the imperfect RIS phase configuration, that causes a drastic reduction of the experienced RIS's RCS. We propose an adaptive RIS alignment procedure to configure the RIS phase for retro-reflection, that caters to mobility. Furthermore, to reduce the implementation cost associated with an RIS-based reflector, we also outline a possible cost-effective realization based on multiple pre-configured SP-EMS modules, whose design is validated with full-wave simulations carried out in Ansys HFSS. Finally, the localization performance of a vehicle equipping a retro-reflecting EMS is assessed in terms of CRB and HCRB in both spatial wideband and narrowband modeling assumptions, the latter used as a benchmark, showing the benefits brought by the employment of a retro-reflective EMS w.r.t. to the case of a bare vehicle.

Appendix A
Hybrid CRB Calculation

For the evaluation of the HCRB, we make reference to the wideband, frequency-dependent signal model in (15). Notice that the RIS position $\mathbf{x}$ can also be treated as a random parameter with a Gaussian a-priori distribution $p(\widehat{\mathbf{x}})$, computing the Bayesian CRB (BCRB). Both HCRB and BCRB are viable options. The observations from the L channels can be stacked into a vector, obtaining

$$\mathbf{y}(f) = \mathbf{a}(f, \boldsymbol{\theta}) + \mathbf{z}(f) \sim \mathcal{CN}(\mathbf{a}(f, \boldsymbol{\theta}), N_0 \mathbf{I}_L \delta(f)) \tag{42}$$

where $\mathbf{a}(f, \boldsymbol{\theta}) \in \mathbb{C}^{L \times 1}$ is the non-linear model relating the parameters to be estimated

$$\boldsymbol{\theta} = [\mathbf{x}^T,\ \overline{\boldsymbol{\xi}}^T]^T \in \mathbb{R}^{6 \times 1} \tag{43}$$

to the observation $\mathbf{y}(f)$, and $\mathbf{z}(f)$ is the additive noise. The set of parameters $\boldsymbol{\theta}$ is herein split between deterministic, namely the RIS position $\mathbf{x}$, and random, namely the RIS angular configuration $\overline{\boldsymbol{\xi}}$. We make the assumption that the orientation of the RIS in space, i.e., angle ψ, is known and does not need to be estimated. The same applies to the amplitude and phase of the scattering coefficient ρ in (4). These assumptions allows retrieving an optimistic PEB. However, the following derivation is general and can be extended to an unknown (but deterministic) orientation of the RIS and scattering amplitude. Notice that modelling $\overline{\boldsymbol{\xi}}$ as a random parameter to be estimated, with an a-priori knowledge of its distribution, is only one of the choices, following from the initial estimation of the RIS position at the vehicle. Alternatively, $\overline{\boldsymbol{\xi}}$ can be assumed as deterministic, whose true value $\overline{\boldsymbol{\xi}} = \boldsymbol{\xi}$ corresponding to the optimal RIS configuration is unknown.

The hybrid information matrix (HIM) $\mathbf{J}_{\mathrm{HCRB}}$ is computed as follows:

$$\mathbf{J}_{\mathrm{HCRB}} = \mathbf{J}_{\mathrm{D}} = \mathbb{E}_{\overline{\boldsymbol{\xi}}}[\mathbf{F}] + \mathbf{J}_{\mathrm{R}} \tag{44}$$

where the first term is the deterministic component of the HIM, obtained by taking the expectation of the Fisher information matrix (FIM) $\mathbf{F}$ over the random parameters $\overline{\boldsymbol{\xi}}$ while $\mathbf{J}_{\mathrm{R}}$ is the additional HIM component due to a-priori knowledge on the random parameters $\overline{\boldsymbol{\xi}}$. The computation of $\mathbf{J}_{\mathrm{R}}$ requires $p(\overline{\boldsymbol{\xi}}) = p(\widehat{\boldsymbol{\xi}})$, i.e., the PDF of the estimated incidence angles onto the RIS, obtained from the position estimation in Section IV knowing the heading ψ.

FIM $\mathbf{F}$ is block-partitioned as follows

$$\mathbf{F} = \begin{bmatrix} \mathbf{F}_{\mathbf{xx}} & \mathbf{F}_{\mathbf{x}\overline{\boldsymbol{\xi}}} \\ \mathbf{F}_{\overline{\boldsymbol{\xi}}\mathbf{x}} & \mathbf{F}_{\overline{\boldsymbol{\xi}}\overline{\boldsymbol{\xi}}} \end{bmatrix} \tag{45}$$

$$\frac{\partial \beta(f,\boldsymbol{\xi}(\mathbf{x}),\bar{\boldsymbol{\xi}})}{\partial \mathbf{x}} = \frac{1}{2\beta^*(f,\boldsymbol{\xi}(\mathbf{x}),\bar{\boldsymbol{\xi}})}\left[\frac{-4c^2}{(4\pi)^3 f_0^2}\frac{\mathbf{x}^T}{\|\mathbf{x}\|^6}\Gamma_{\mathrm{ris}}(f,\boldsymbol{\xi}(\mathbf{x}),\bar{\boldsymbol{\xi}}) + \frac{c^2}{(4\pi)^3 f_0^2\|\mathbf{x}\|^4}\frac{\partial \Gamma_{\mathrm{ris}}(f,\boldsymbol{\xi}(\mathbf{x}),\bar{\boldsymbol{\xi}})}{\partial \mathbf{x}}\right] \in \mathbb{C}^{1\times 3} \tag{49}$$

$$\frac{\partial \beta(f,\boldsymbol{\xi}(\mathbf{x}),\bar{\boldsymbol{\xi}})}{\partial \bar{\boldsymbol{\xi}}} = \frac{1}{2\beta^*(f,\boldsymbol{\xi}(\mathbf{x}),\bar{\boldsymbol{\xi}})}\left[\frac{c^2}{(4\pi)^3 f_0^2\|\mathbf{x}\|^4}\frac{\partial \Gamma_{\mathrm{ris}}(f,\boldsymbol{\xi}(\mathbf{x}),\bar{\boldsymbol{\xi}})}{\partial \bar{\boldsymbol{\xi}}}\right] \in \mathbb{C}^{1\times 2} \tag{50}$$

$$\frac{\partial}{\partial \mathbf{x}}\left(e^{-j2\pi(f_0+f)(2\tau_0+\Delta\boldsymbol{\tau}_i+\Delta\boldsymbol{\tau}_o)}\right) = e^{-j2\pi(f_0+f)(2\tau_0+\Delta\boldsymbol{\tau}_i+\Delta\boldsymbol{\tau}_o)} \odot [-j2\pi(f_0+f)]\frac{\partial}{\partial \mathbf{x}}(2\tau_0+\Delta\boldsymbol{\tau}_i+\Delta\boldsymbol{\tau}_o) \in \mathbb{C}^{L\times 3} \tag{51}$$

with straightforward dimensions, whose entries are

$$\mathbf{F}_{\boldsymbol{\mu}\boldsymbol{\nu}} = \frac{2}{N_0}\Re\left\{\int_{-B/2}^{B/2}\left(\frac{\partial \mathbf{a}(f,\boldsymbol{\theta})}{\partial \boldsymbol{\mu}}\right)^H \frac{\partial \mathbf{a}(f,\boldsymbol{\theta})}{\partial \boldsymbol{\nu}} df\right\} \tag{46}$$

where $\boldsymbol{\mu}$ and $\boldsymbol{\nu}$ can be any set of the parameters to be estimated, i.e., $\mathbf{x}$, $\bar{\boldsymbol{\xi}}$. Single FIM terms are:

$$\begin{aligned}\frac{\partial \mathbf{a}(f,\boldsymbol{\theta})}{\partial \mathbf{x}} =& S(f)\frac{\partial \beta(f,\boldsymbol{\xi}(\mathbf{x}),\bar{\boldsymbol{\xi}})}{\partial \mathbf{x}} e^{-j2\pi(f_0+f)(2\tau_0+\Delta\boldsymbol{\tau}_i+\Delta\boldsymbol{\tau}_o)} + \\ & S(f)\beta(f,\boldsymbol{\xi}(\mathbf{x}),\bar{\boldsymbol{\xi}})\frac{\partial}{\partial \mathbf{x}}\left[e^{-j2\pi(f_0+f)(2\tau_0+\Delta\boldsymbol{\tau}_i+\Delta\boldsymbol{\tau}_o)}\right]\end{aligned} \tag{47}$$

$$\frac{\partial \mathbf{a}(f,\boldsymbol{\theta})}{\partial \bar{\boldsymbol{\xi}}} = S(f)\frac{\partial \beta(f,\boldsymbol{\xi}(\mathbf{x}),\bar{\boldsymbol{\xi}})}{\partial \bar{\boldsymbol{\xi}}} e^{-j2\pi(f_0+f)(2\tau_0+\Delta\boldsymbol{\tau}_i+\Delta\boldsymbol{\tau}_o)} \tag{48}$$

where single gradients are detailed in (49), (50) and (51). The inverse of the FIM $\mathbf{F}$ provides the CRB for deterministic parameters, namely $\mathbf{C}_{\mathrm{CRB}} = \mathbf{F}^{-1}$.

A. CRB for Perfect RIS Configuration $\bar{\boldsymbol{\xi}} = \boldsymbol{\xi}$

A further useful performance bound is to consider the perfect configuration of the RIS ($\bar{\boldsymbol{\xi}} = \boldsymbol{\xi}$), e.g., achieved with a reflection beam sweeping procedure in Section IV. In this case, the only parameter to be estimated is $\mathbf{x}$, as the residual uncertainty on $\bar{\boldsymbol{\xi}}$ is zero, or it can be approximated as zero. The HCRB therefore degenerates to the CRB for the FIM:

$$\mathbf{F}^{\mathrm{u}} = \mathbf{F}_{\mathbf{x}\mathbf{x}} \tag{52}$$

and we have $\mathbf{C}_{\mathrm{HCRB}} \succeq \mathbf{C}^{\mathrm{u}}_{\mathrm{CRB}} = (\mathbf{F}^{\mathrm{u}})^{-1}$ as the uncertainty of the RIS configuration angles is removed from the FIM in (45) and cannot affect the estimation of the other parameters.

REFERENCES

[1] W. Jiang, B. Han, M. A. Habibi, and H. D. Schotten, "The Road Towards 6G: A Comprehensive Survey," *IEEE Open Journal of the Communications Society*, vol. 2, pp. 334–366, 2021.

[2] H. Wymeersch, A. Pärssinen, T. E. Abrudan, A. Wolfgang, K. Haneda, M. Sarajlic, M. E. Leinonen, M. F. Keskin, H. Chen, S. Lindberg, P. Kyösti, T. Svensson, and X. Yang, "6G Radio Requirements to Support Integrated Communication, Localization, and Sensing," in *2022 Joint European Conference on Networks and Communications & 6G Summit (EuCNC/6G Summit)*, 2022, pp. 463–469.

[3] M. A. Uusitalo, P. Rugeland, M. R. Boldi, E. C. Strinati, P. Demestichas, M. Ericson, G. P. Fettweis, M. C. Filippou, A. Gati, M.-H. Hamon, M. Hoffmann, M. Latva-Aho, A. Pärssinen, B. Richerzhagen, H. Schotten, T. Svensson, G. Wikström, H. Wymeersch, V. Ziegler, and Y. Zou, "6G Vision, Value, Use Cases and Technologies From European 6G Flagship Project Hexa-X," *IEEE Access*, vol. 9, pp. 160 004–160 020, 2021.

[4] M. Di Renzo, A. Zappone, M. Debbah, M.-S. Alouini, C. Yuen, J. De Rosny, and S. Tretyakov, "Smart radio environments empowered by reconfigurable intelligent surfaces: How it works, state of research, and the road ahead," *IEEE Journal on Selected Areas in Communications*, vol. 38, no. 11, pp. 2450–2525, 2020.

[5] G. Oliveri, D. H. Werner, and A. Massa, "Reconfigurable electromagnetics through metamaterials—a review," *Proceedings of the IEEE*, vol. 103, no. 7, pp. 1034–1056, 2015.

[6] Y. Liu, X. Liu, X. Mu, T. Hou, J. Xu, M. Di Renzo, and N. Al-Dhahir, "Reconfigurable intelligent surfaces: Principles and opportunities," *IEEE Communications Surveys Tutorials*, vol. 23, no. 3, pp. 1546–1577, 2021.

[7] K. Keykhosravi, B. Denis, G. C. Alexandropoulos, Z. S. He, A. Albanese, V. Sciancalepore, and H. Wymeersch, "Leveraging RIS-Enabled Smart Signal Propagation for Solving Infeasible Localization Problems: Scenarios, Key Research Directions, and Open Challenges," *IEEE Vehicular Technology Magazine*, vol. 18, no. 2, pp. 20–28, 2023.

[8] S. Hu, F. Rusek, and O. Edfors, "Beyond Massive MIMO: The Potential of Positioning With Large Intelligent Surfaces," *IEEE Transactions on Signal Processing*, vol. 66, no. 7, pp. 1761–1774, 2018.

[9] H. Zhang, B. Di, K. Bian, Z. Han, H. V. Poor, and L. Song, "Toward ubiquitous sensing and localization with reconfigurable intelligent surfaces," *Proceedings of the IEEE*, vol. 110, no. 9, pp. 1401–1422, 2022.

[10] S. Buzzi, E. Grossi, M. Lops, and L. Venturino, "Radar Target Detection Aided by Reconfigurable Intelligent Surfaces," *IEEE Signal Processing Letters*, vol. 28, pp. 1315–1319, 2021.

[11] ——, "Foundations of MIMO Radar Detection Aided by Reconfigurable Intelligent Surfaces," *IEEE Transactions on Signal Processing*, vol. 70, pp. 1749–1763, 2022.

[12] G. Mylonopoulos, C. D'Andrea, and S. Buzzi, "Active Reconfigurable Intelligent Surfaces for User Localization in mmWave MIMO Systems," in *2022 IEEE 23rd International Workshop on Signal Processing Advances in Wireless Communication (SPAWC)*, 2022, pp. 1–5.

[13] A. Elzanaty, A. Guerra, F. Guidi, and M.-S. Alouini, "Reconfigurable Intelligent Surfaces for Localization: Position and Orientation Error Bounds," *IEEE Transactions on Signal Processing*, vol. 69, pp. 5386–5402, 2021.

[14] A. Aubry, A. De Maio, and M. Rosamilia, "RIS-Aided Radar Sensing in N-LOS Environment," in *2021 IEEE 8th International Workshop on Metrology for AeroSpace (MetroAeroSpace)*, 2021, pp. 277–282.

[15] T. Ma, Y. Xiao, X. Lei, W. Xiong, and Y. Ding, "Indoor localization with reconfigurable intelligent surface," *IEEE Communications Letters*, vol. 25, no. 1, pp. 161–165, 2021.

[16] Z. Zhang, T. Jiang, and W. Yu, "Active sensing for localization with reconfigurable intelligent surface," *ICC 2023 - IEEE International Conference on Communications*, pp. 4261–4266, 2023. [Online]. Available: https://api.semanticscholar.org/CorpusID:259325852

[17] X. Pang, W. Mei, N. Zhao, and R. Zhang, "Cellular sensing via cooperative intelligent reflecting surfaces," *IEEE Transactions on Vehicular Technology*, vol. 72, no. 11, pp. 15 086–15 091, 2023.

[18] H. Zhang, H. Zhang, B. Di, K. Bian, Z. Han, and L. Song, "MetaLocalization: Reconfigurable Intelligent Surface Aided Multi-User Wireless Indoor Localization," *IEEE Transactions on Wireless Communications*, vol. 20, no. 12, pp. 7743–7757, 2021.

[19] ——, "MetaRadar: Multi-target Detection for Reconfigurable Intelligent Surface Aided Radar Systems," *IEEE Transactions on Wireless Communications*, pp. 1–1, 2022.

[20] Z. Wang, Z. Liu, Y. Shen, A. Conti, and M. Z. Win, "Location Awareness in Beyond 5G Networks via Reconfigurable Intelligent Surfaces," *IEEE Journal on Selected Areas in Communications*, vol. 40, no. 7, pp. 2011–2025, 2022.

[21] F. Jiang, A. Abrardo, K. Keykhoshravi, H. Wymeersch, D. Dardari, and M. Di Renzo, "Two-Timescale Transmission Design and RIS Optimization for Integrated Localization and Communications," *IEEE Transactions on Wireless Communications*, pp. 1–1, 2023.

[22] P. Zheng, H. Chen, T. Ballal, H. Wymeersch, and T. Y. Al-Naffouri, "Misspecified Cramér-Rao Bound of RIS-Aided Localization Under Geometry Mismatch," in *ICASSP 2023 - 2023 IEEE International Conference on Acoustics, Speech and Signal Processing (ICASSP)*, 2023, pp. 1–5.

[23] Z. Wang, Z. Liu, Y. Shen, A. Conti, and M. Z. Win, "Source Localization with Intelligent Surfaces," in *ICC 2022 - IEEE International Conference on Communications*, 2022, pp. 895–900.

[24] G. Oliveri, M. Salucci, and A. Massa, "Generalized Analysis and Unified Design of EM Skins," *IEEE Transactions on Antennas and Propagation*, vol. 71, no. 8, pp. 6579–6592, 2023.

[25] D. Dardari, N. Decarli, A. Guerra, and F. Guidi, "LOS/NLOS Near-Field Localization With a Large Reconfigurable Intelligent Surface," *IEEE Transactions on Wireless Communications*, vol. 21, no. 6, pp. 4282–4294, 2022.

[26] M. Luan, B. Wang, Y. Zhao, Z. Feng, and F. Hu, "Phase Design and Near-Field Target Localization for RIS-Assisted Regional Localization System," *IEEE Transactions on Vehicular Technology*, vol. 71, no. 2, pp. 1766–1777, 2022.

[27] O. Rinchi, A. Elzanaty, and M.-S. Alouini, "Compressive Near-Field Localization for Multipath RIS-Aided Environments," *IEEE Communications Letters*, vol. 26, no. 6, pp. 1268–1272, 2022.

[28] X. Zhang and H. Zhang, "Hybrid reconfigurable intelligent surfaces-assisted near-field localization," *IEEE Communications Letters*, vol. 27, no. 1, pp. 135–139, 2023.

[29] K. Keykhosravi, M. F. Keskin, S. Dwivedi, G. Seco-Granados, and H. Wymeersch, "Semi-Passive 3D Positioning of Multiple RIS-Enabled Users," *IEEE Transactions on Vehicular Technology*, vol. 70, no. 10, pp. 11 073–11 077, 2021.

[30] R. Ghazalian, K. Keykhosravi, H. Chen, H. Wymeersch, and R. Jäntti, "Bi-Static Sensing for Near-Field RIS Localization," in *GLOBECOM 2022 - 2022 IEEE Global Communications Conference*, 2022, pp. 6457–6462.

[31] P. Wang, W. Mei, J. Fang, and R. Zhang, "Target-mounted intelligent reflecting surface for joint location and orientation estimation," *IEEE Journal on Selected Areas in Communications*, vol. 41, no. 12, pp. 3768–3782, 2023.

[32] K. Keykhosravi, M. F. Keskin, G. Seco-Granados, P. Popovski, and H. Wymeersch, "RIS-Enabled SISO Localization Under User Mobility and Spatial-Wideband Effects," *IEEE Journal of Selected Topics in Signal Processing*, vol. 16, no. 5, pp. 1125–1140, 2022.

[33] D. Tagliaferri, M. Mizmizi, S. Mura, and U. Spagnolini, "RIS Localization and Spatially Wideband Filtering Effects," in *ICASSP 2024 - 2024 IEEE International Conference on Acoustics, Speech and Signal Processing (ICASSP)*, 2024, pp. 8961–8965.

[34] N. Garcia, A. Fascista, A. Coluccia, H. Wymeersch, C. Aydogdu, R. Mendrzik, and G. Seco-Granados, "Cramér-rao bound analysis of radars for extended vehicular targets with known and unknown shape," *IEEE Transactions on Signal Processing*, vol. 70, pp. 3280–3295, 2022.

[35] A. F. García-Fernández, J. L. Williams, L. Svensson, and Y. Xia, "A poisson multi-bernoulli mixture filter for coexisting point and extended targets," *IEEE Transactions on Signal Processing*, vol. 69, pp. 2600–2610, 2021.

[36] M. Naraghi, W. Stromberg, and M. Daily, "Geometric rectification of radar imagery using digital elevation models," *Photogrammetric Engineering and Remote Sensing*, vol. 49, no. 2, pp. 195–199, 1983.

[37] M. Mizmizi, R. A. Ayoubi, D. Tagliaferri, K. Dong, G. G. Gentili, and U. Spagnolini, "Conformal metasurfaces: A novel solution for vehicular communications," *IEEE Transactions on Wireless Communications*, vol. 22, no. 4, pp. 2804–2817, 2023.

[38] D. Tagliaferri, M. Mizmizi, R. A. Ayoubi, G. G. Gentili, and U. Spagnolini, "Conformal Intelligent Reflecting Surfaces for 6G V2V Communications," in *2022 1st International Conference on 6G Networking (6GNet)*, 2022, pp. 1–8.

[39] M. Mizmizi, D. Tagliaferri, M. Khosronejad, L. Resteghini, G. G. Gentili, L. Draghi, and U. Spagnolini, "Conformal Metasurfaces for Recovering Dynamic Blockage in Vehicular Systems," in *GLOBECOM 2022 - 2022 IEEE Global Communications Conference*, 2022, pp. 6025–6030.

[40] D. Desai, I. Gatley, C. Bolton, L. Rizzo, S. Gatley, and J. F. Federici, "Terahertz van atta retroreflecting arrays," *Journal of Infrared, Millimeter, and Terahertz Waves*, pp. 1–12, 2020.

[41] G. Oliveri, F. Zardi, P. Rocca, M. Salucci, and A. Massa, "Building a smart em environment - ai-enhanced aperiodic micro-scale design of passive em skins," *IEEE Transactions on Antennas and Propagation*, vol. 70, no. 10, pp. 8757–8770, 2022.

[42] ——, "Constrained Design of Passive Static EM Skins," *IEEE Transactions on Antennas and Propagation*, vol. 71, no. 2, pp. 1528–1538, 2023.

[43] G. Oliveri, P. Rocca, M. Salucci, and A. Massa, "Holographic Smart EM Skins for Advanced Beam Power Shaping in Next Generation Wireless Environments," *IEEE Journal on Multiscale and Multiphysics Computational Techniques*, vol. 6, pp. 171–182, 2021.

[44] H. Messer, "The Hybrid Cramer-Rao Lower Bound - From Practice to Theory," in *Fourth IEEE Workshop on Sensor Array and Multichannel Processing, 2006.*, 2006, pp. 304–307.

[45] 3GPP TR 37.885 v15.3., "Study on evaluation methodology of new V2X use cases for LTE and NR - 3rd Generation Partnership Project (3GPP)," 2019.

[46] F. Folster and H. Rohling, "Data association and tracking for automotive radar networks," *IEEE Transactions on Intelligent Transportation Systems*, vol. 6, no. 4, pp. 370–377, 2005.

[47] K. Granström, M. Fatemi, and L. Svensson, "Poisson multi-bernoulli mixture conjugate prior for multiple extended target filtering," *IEEE Transactions on Aerospace and Electronic Systems*, vol. 56, no. 1, pp. 208–225, 2020.

[48] B.-N. Vo, B.-T. Vo, N.-T. Pham, and D. Suter, "Joint detection and estimation of multiple objects from image observations," *IEEE Transactions on Signal Processing*, vol. 58, no. 10, pp. 5129–5141, 2010.

[49] J. J. M. de Wit, W. L. van Rossum, and A. J. de Jong, "Orthogonal Waveforms for FMCW MIMO Radar," in *2011 IEEE RadarCon (RADAR)*, 2011, pp. 686–691.

[50] S. Fan, W. Ni, H. Tian, Z. Huang, and R. Zeng, "Carrier Phase-Based Synchronization and High-Accuracy Positioning in 5G New Radio Cellular Networks," *IEEE Transactions on Communications*, vol. 70, no. 1, pp. 564–577, 2022.

[51] B. Wang, F. Gao, S. Jin, H. Lin, G. Y. Li, S. Sun, and T. S. Rappaport, "Spatial-wideband effect in massive mimo with application in mmwave systems," *IEEE Communications Magazine*, vol. 56, no. 12, pp. 134–141, 2018.

[52] F. Ulaby, D. Long, C. Elachi, and K. Sarabandi, *Microwave Radar and Radiometric Remote Sensing*. University of Michigan Press, 2014. [Online]. Available: https://books.google.it/books?id=y6pZngEACAAJ

[53] F. Costa and M. Borgese, "Electromagnetic Model of Reflective Intelligent Surfaces," *IEEE Open Journal of the Communications Society*, vol. 2, pp. 1577–1589, 2021.

[54] O. Ozdogan, E. Bjornson, and E. G. Larsson, "Intelligent reflecting surfaces: Physics, propagation, and pathloss modeling," *IEEE Wireless Communications Letters*, vol. 9, no. 5, pp. 581–585, 2020.

[55] S. Ellingson, "Path loss in reconfigurable intelligent surface-enabled channels," in *2021 IEEE 32nd Annual International Symposium on Personal, Indoor and Mobile Radio Communications (PIMRC)*, 2021, pp. 829–835.

[56] T. Instruments, "Imaging radar using cascaded mmwave sensor reference design," available at: https://www.ti.com/lit/ug/tiduen5a/tiduen5a.pdf.

[57] M. Skolnik, *Introduction to Radar Systems*. London: McGraw-Hill Education, 2002.

[58] "Remcom WaveFarer," https://www.remcom.com/wavefarer-automotive-radar-software, Accessed on May 2023.

[59] H. Wymeersch, R. Amiri, and G. Seco-Granados, "Fundamental performance bounds for carrier phase positioning in cellular networks," 2023.

[60] U. Spagnolini, *Statistical Signal Processing in Engineering*. John Wiley & Sons Ltd, 2018.